Journal of Manufacturing Processes 172 (2026) 558–577

Contents lists available at ScienceDirect

Journal of Manufacturing Processes

journal homepage: www.elsevier.com/locate/manpro

In-process optical measurement and compensation of machine tool thermal deformations

Zongze Li [a,b,c,*], Aaron Cornelius [d], Gonzalo Reyes [c], Edward C. Kinzel [c], Ryuta Sato [b], Gregory W. Vogl [d], Robert G. Landers [c]

[a] Graduate School of Advanced Science and Engineering, Hiroshima University, Kagamiyama 1-4-1, Higashi-Hiroshima, 739-8527, Japan
[b] Graduate School of Engineering, Nagoya University, Furo-cho, Chikusa-ku, Nagoya, 464-8603, Japan
[c] Department of Aerospace and Mechanical Engineering, University of Notre Dame, 365 Fitzpatrick Hall of Engineering, Notre Dame, IN, 46556, USA
[d] Engineering Laboratory, National Institute of Standards and Technology, 100 Bureau Drive, Stop 8220, Gaithersburg, MD, 20899, USA

HIGHLIGHTS

- In-process strategy to measure and compensate machine tool thermal errors is proposed.
- The measurement method is implemented in-process.
- Uncertainty sources for optical measurement methods are discussed and analyzed.
- The proposed method is validated for two different operations on two different machine tools.

GRAPHICAL ABSTRACT

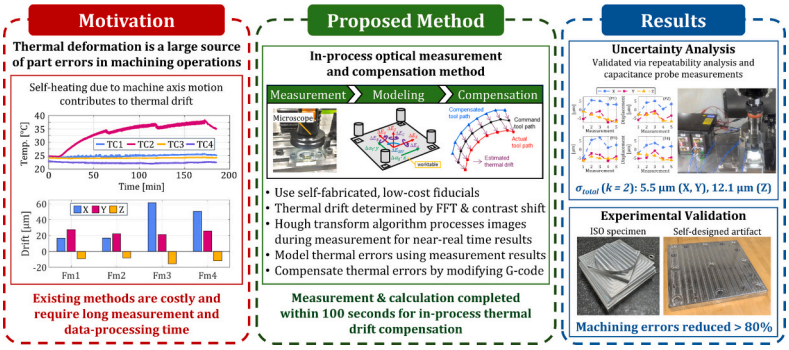

ARTICLE INFO

Keywords:
Machine tool thermal deformations
Three-dimensional optical measurement
In-process compensation

ABSTRACT

Machine tool deformations due to thermal loads from motors and part processing, as well as from changing ambient temperature, can dominate the machine tool's volumetric error and substantially affect part quality. Current methods struggle to take measurements and adjust toolpaths quickly enough for in-process corrections and, thus, few experimental results for machining operations have been reported. This paper describes an in-process strategy to measure, model, and compensate machine tool thermal errors. Thermal drifts are measured via a digital microscope mounted in the spindle. A thermal drift prediction model is constructed based on those measurements, and the results are used to modify the G-code to compensate for the errors. Two implementations of the strategy are considered. The timing requirements of previously proposed measurement methods are improved in the first implementation using a two-dimensional Fast Fourier Transformation (2D-FFT) method and in the second implementation by employing a Hough Transformation method. In both implementations, the entire process from measurement to compensation requires less than 100 s, making the proposed method applicable for in-process machine tool thermal error compensation. Uncertainty sources for both methods are discussed and analyzed. The strategy is demonstrated with an experimental study of a scaled ISO

* Corresponding author at: Graduate School of Advanced Science and Engineering, Hiroshima University, Kagamiyama 1-4-1, Higashi-Hiroshima, 739-8527, Japan.
E-mail address: zzli@hiroshima-u.ac.jp (Z. Li).

https://doi.org/10.1016/j.jmapro.2026.05.074
Received 26 February 2026; Received in revised form 22 May 2026; Accepted 26 May 2026
Available online 9 June 2026

10791-7 M1 specimen and a second experimental study of a larger artifact with a grid of bores. It was found that the thermal error compensation methodology reduces errors on machined parts by up to an order of magnitude compared to parts machined without compensation, with residual errors below the measurement uncertainty.

1. Introduction

The increasing need for greater product quality and variety has created a growing demand for greater machine tool precision and, thus, the elimination or correction of error sources that give rise to decreased precision. The error sources include geometric (e.g., assembly errors), process (e.g., tool deflections), motion system (e.g., contour errors), and thermal-induced (e.g., structural thermal expansion). While the specific contribution of these error sources depends on the machine tool, environmental conditions, and process, in many situations thermal-induced errors are one of the most significant error sources contributing to part inaccuracy, especially for large machine tools [1,2]. Although thermal-induced errors can be reduced by designing machine tools to be less sensitive to the inner and ambient temperature variations [3,4], this is a very costly solution [5] and prone to modeling errors, which are prevalent in thermal models of complex machines. Therefore, there is a need for efficient methods to compensate thermal-induced errors which can be applied to improve the accuracy of existing machine tools.

Another common method to reduce machine tool thermal-induced errors is through compensation. Typically, compensation methods either 1) measure the machine tool temperature variations (indirect measurement) or 2) measure the drifts of the tool center point (TCP) due to temperature variations (direct measurement). A predictive model (e.g., linear regression [6], finite element [7], or neural network models [8]) then estimates the TCP errors throughout the work volume. Compensation values are calculated based on the predictive model and applied to the tool path to reduce the effect of the thermal-induced errors.

Indirect measurement techniques measure the machine thermal state and estimate machine deformations using a model [9,10]. However, these methods usually lack the necessary accuracy [7,11] and cannot meet the timing requirements for in-process compensation. In addition, the temperature-sensitive points are different for each machine and thermal condition [12], so models cannot be generally applied across a wide variety of machine tools.

Direct measurement techniques typically measure thermal-induced TCP errors using specialized displacement measurement instruments, such as laser interferometers [13], capacitive sensor [14], touch-trigger probes [15], R-test system [16], double ball-bars [17], etc. When using direct measurement techniques, many measurements must be taken to fully map the work volume. Therefore, rapid and accurate measurement techniques are required. Ibaraki et al. [18] and Mori et al. [19] measured thermal-induced errors of a five-axis machine tool using a laser-tracking interferometer, achieving an accuracy of 10 μm in less than 7 min. Brecher et al. [20] designed a thermally-stable laser frame and spindle-mounted tool-changeable position-sensing detector, which was able to measure thirteen error motions in 4 min. Gomez-Acedo et al. [21] proposed a multilateration strategy to measure the thermal distortion of large machine tools with a laser tracking interferometer, and were able to measure 12 target points on the machine frame in 30 min. Mutilba et al. [22] synchronized and automated the multilateration method for laser trackers, reducing overall measurement time for 96 length measurements to 8 min. Although these methods can achieve rapid high-precision measurements, specialized measurement instruments tend to be very expensive and can require extensive set up time, and the multi-minute measurement times may still not be suitable for measuring dynamic thermal errors mid-process.

Thermal-induced errors can also be evaluated by comparing the machining accuracies of fabricated specimens in different machine tool thermal conditions. Ibaraki and Ota [23], Ibaraki and Okumura [24], and Cheng et al. [25] proposed several machining tests to evaluate thermal-induced errors; however, these methods require a long measurement times and are not suitable for measuring and compensating thermal errors in-process.

Vision-based systems are increasingly being applied to take quick measurements of thermal-induced errors [26]. Irino et al. [27] used multiple cameras to observe orthogonal grid patterns mounted on the worktable and measure positional and angular errors. The proposed method was roughly twice as fast as a laser tracker with equivalent accuracy. Hartlieb et al. [28] used a two-camera system to measure the position of light-emitting diodes (LEDs) in the work volume, achieving a sub-micrometer level measurement accuracy. Li et al. [29] measured and compensated two dimensional contouring errors by measuring novel patterns using an industrial vision camera, with an accuracy of 4 μm over a 230 mm square fiducial. However, these methods can only measure the error components perpendicular to the camera center line (in-plane errors). The requirement for multiple cameras makes these systems more difficult to set up and use for in-process compensation. Zhang et al. [30] proposed a perspective-based homography approach which measures three-dimensional positioning errors with a single camera, reaching an accuracy of 10 μm. However, this method required a large 150 mm measurement target mounted to the spindle and extensive calculation time, posing challenges for in-process compensation.

To measure thermal errors using only one camera, Vogl et al. [31] and Li et al. [32] utilized a low-cost spindle-mounted microscope to measure fiducials mounted to the worktable. This approach used the shift in the microscope's focal plane relative to the fiducial to measure the three-dimensional positional deviation between the spindle and worktable, with an accuracy of 1 μm. The measured errors were incorporated into a regression-based error model. However, neither study provided a full uncertainty budget or demonstrated the ability to compensate thermal errors via actual machining tests. Furthermore, these methods used relatively expensive fiducials and required long measurement and computation times [31,32] (6.5 and 4.5 min, respectively). As such, these methods were not suitable for low-cost measurement and compensation of thermal errors in near real-time. A graphic summary of thermal error measurement and compensation methods and their challenges is shown as Fig. 1.

The novel contributions of this study are 1) an in-process optical measurement and compensation strategy for machine tool thermal-induced errors, 2) the analysis of measurement uncertainties in optical measurement techniques for thermal induced errors in machine tools, and 3) the implementation of the strategy during actual machining experiments. To address the limitations of [31,32], two measurement methods were implemented to reduce the strategy's measurement and computation time and allow for in-process implementation. In the first method, self-fabricated low-cost fiducials with non-periodic-patterns are utilized instead of commercial high-precision fiducials, and the displacement between images is extracted using a Fast Fourier Transform (FFT) algorithm, allowing an overall data-processing time of 34.2 s for four fiducials. In the experimental verification, Method I can complete a full measurement routine in less than 100 s, including data-processing and feed-axis translations. The second method uses the same general fiducials and measurement procedures as [31] but uses an optimized data processing pipeline to automatically process incoming data during the measurement process, reducing the overall data-processing time to 8.5 s for four fiducials. In the experimental verification, Method II completes a full measurement routine in 85 s, including data-processing. The measured thermal errors are then used to construct

a kinematic error model, and the G-code is modified by inverting the model. Uncertainty analyses were conducted to understand and quantify the various error sources. In two machining experiments, the proposed measurement and compensation strategy was shown to compensate thermal-induced errors on fabricated parts to within the measurement uncertainty. Further, the entire process was completed within 100 s, making it suitable for in-process thermal error compensation. The measurement and compensation strategy does not require specialized instruments (e.g., laser interferometers), making it a low-cost, efficient tool for industrial usage. This method concentrates on error sources which cause relative errors in the machine tool static positioning like thermal drift, and cannot measure other errors which manifest solely during motion or cutting (e.g., dynamic errors due to cutting forces).

The remainder of this paper is as follows: Section 2 presents an overview of the proposed measurement/compensation strategy. Section 3 introduces two methods for in-process measurement and discusses how they provide real-time data-processing, and the algorithm-induced uncertainty analyses are conducted. The experimental validations and corresponding discussions of the two methods are given in Sections 4 and 5. Conclusions and future work are given in Section 6.

2. In-process measurement and compensation strategy

An overview of the proposed strategy is introduced in this section. The measurement methods determine drifts of the spindle relative to the worktable due to thermal deformation (referred to as thermal drifts). For this purpose, the fiducials are fixed onto the worktable when the machine tool is in cold state (considered as no thermal deformation and hereinafter referred to as State 1) and measured once as the reference, and then kept mounted during the machining process. Thermal deformation may occur after a long period of machining, and thus, the fiducials are measured again, hereinafter referred to as State 2, such that the thermal drifts from State 2 to State 1 are determined. Using the measured thermal drifts, an error model estimating the thermal drifts of all TCPs among the workspace is constructed, and the error compensation is subsequently conducted by modifying the G-code with the inverse error model.

2.1. Measurement of thermal drifts

The basic measurement principle is illustrated in Fig. 2. When the machine tool thermal state varies, the relative position between the spindle and the worktable changes due to thermal deformations of the machine tool structure. To capture these deviations, a microscope is mounted in the spindle and fiducials are mounted on the worktable. The fiducials are measured before machine tool thermal deformation (i.e., in the cold state) and are measured during the operation to determine thermal errors. In this study, these relative positional deviations are denoted thermal drifts, an example of which is illustrated in Fig. 2(a). In the microscope view, the deviations perpendicular to the spindle centerline, i.e., XY-plane of the machine tool coordinate frame (MCF), are denoted in-plane deviations and are observed by measuring pattern positional shifts, as shown in Fig. 2(b). The deviations along the spindle centerline, i.e., Z-axis of the MCF, are denoted out-of-plane deviations and are observed by measuring variations in the image focus, as shown in Fig. 2(c).

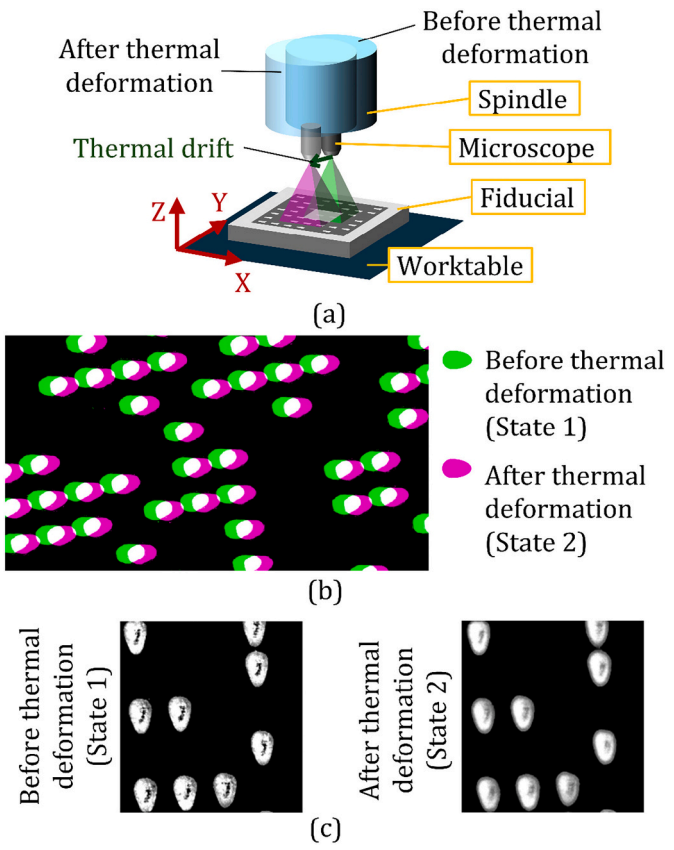

Fig. 2. Measurement principle. (a) Illustration of the machine tool thermal drift where the microscope and the fiducial are fixed to the spindle and worktable, respectively, and the drifts are indicated as (b) in-plane deviation where the pattern positions are shifted; and (c) out-of-plane deviations where the images before and after thermal deformations are in and out of focus, respectively, due to the Z-axial drifts. The coordinate frame attached to the worktable in (a) is the machine tool coordinate frame (MCF).

The fiducials and their placement on the machine tool worktable are shown in Fig. 3. Fiducials are categorized as either the Calibration

Method	Machine Tool Design	Indirect Measurement	Direct Measurement		
			Machining Tests	Specialized Instruments	Vision-Based System
Challenge	• Expensive • Lack necessary accuracy • Cannot be utilized on existing machine tools	• Lack necessary accuracy • Time consuming • Sensitive points vary with machine	• Requires extensive testing before use • Cannot measure general thermal errors	• Expensive • Long set up time • Cannot be implemented during machining operation	• Expensive equipment typically used • Long data processing time typically required

Fig. 1. Thermal error measurement and compensation methods and their challenges. This paper seeks to address the challenges of vision-based systems.

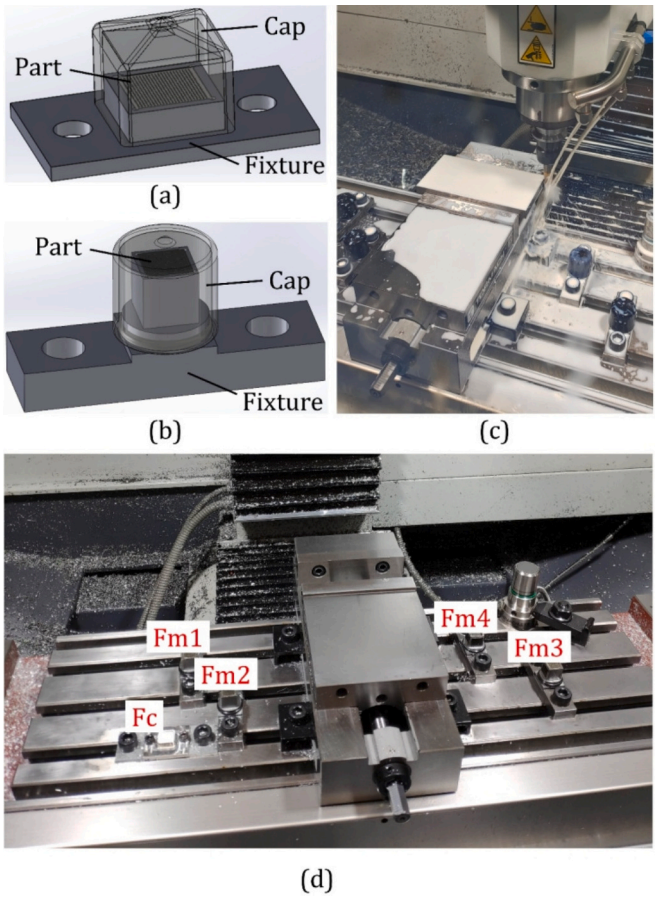

Fig. 3. Fiducials and their placements for the Method I (see Section 3.1) as a sample. (a) and (b) are the computer-aided design (CAD) model of Calibration Fiducial (Fc) and Measurement Fiducial (Fm), respectively, of which the fixtures are fabricated oversize to the cap to make sealing better. (c) is the appearance of real machining without fiducials dismounted, and the design can prevent the Part from coolant and cutting chips. (d) is the placement of the fiducials.

Fiducial (Fc), which is utilized for measurement calibration, e.g., pixel length, or as a Measurement Fiducial (Fm), which is utilized to determine thermal drifts. Note that the Fc needs to be high-precision, while the Fm can be low-precision, and Fc can be used for any Fm. Each fiducial consists of three components: the Part, which is the substrate with the pattern to be imaged by the microscope; the Fixture, which holds the Part and is mounted on the worktable; and the Cap, which is used for sealing, as shown in Fig. 3(a, b). Multiple Fms are utilized to measure the thermal drifts across the workspace. When each fiducial is first attached to the worktable, the operator manually determines the nominal location in the MCF by jogging the feed axes until the microscope view gets in focus. During measurement, it is important that the fiducials are clean of chips and coolant since those can affect the optical measurements. For Method I, caps were attached to the fiducials during machining to prevent the Part from coolant and chip contamination, as shown in Fig. 3(c). When taking measurements, the caps are removed from the fiducials, as shown in Fig. 3(d). For Method II, the fiducials were instead left exposed during machining and cleaned with ethanol prior to measurements.

2.2. Error model with measured thermal drifts

A kinematic model is constructed to estimate thermal drifts within the machine workspace, as illustrated as Fig. 4(a). The relationship between the actual and nominal (i.e., commanded) TCPs is

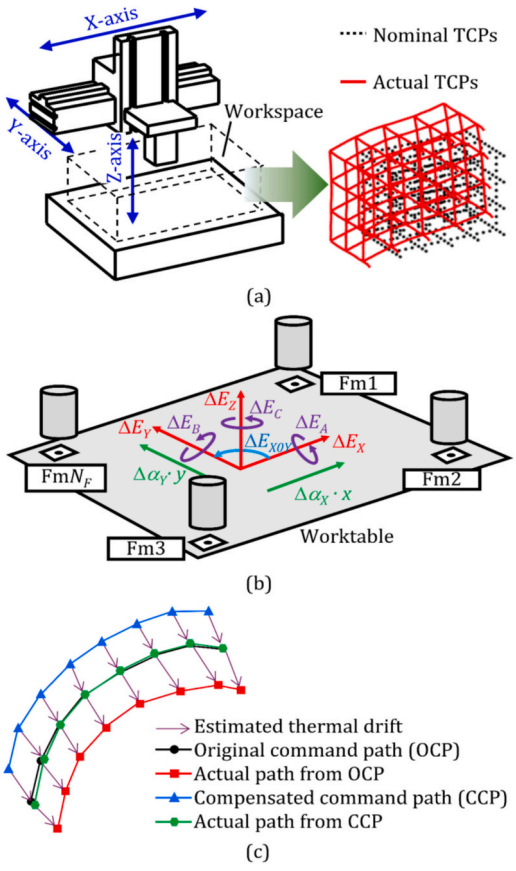

Fig. 4. (a) Illustration of thermal drifts throughout the machine tool workspace where the drifts are the positional deviations between nominal and actual TCPs; (b) illustration of the adopted error model in this work which kinematically estimates the thermal drifts of each TCP, where $\Delta E_{X,Y,Z}$ denote the position errors along X-, Y-, and Z-axes, respectively, $\Delta E_{A,B,C}$ denote the orientation errors around the X-, Y-, and Z-axes, respectively, ΔE_{X0Y} denotes the squareness between the X- and Y- axes, and $\Delta\alpha_{X,Y}$ denote the linear thermal expansions along the X- and Y-axes, respectively [33]; and (c) illustrates the G-code modification (the actual path from the OCP, due to thermal drift, is estimated using the error model. Based on the inverted error model, the CCP is computed such that the actual path from the CCP coincides with the OCP).

$$[\,x_a \quad y_a \quad z_a \quad 1\,]^T = \mathbf{M}[\,x_n \quad y_n \quad z_n \quad 1\,]^T \tag{1}$$

where $[x_n, y_n, z_n]^T$ and $[x_a, y_a, z_a]^T$ are the vectors of the nominal and actual TCPs, respectively, and **M** is the error model. This study adopts a nine-parameter error model [31,32] that accounts for position errors along the axes, rotational errors about the axes, squareness between the X- and Y-axes, and linear thermal expansion along the X- and Y-axes. The error model parameters are illustrated in Fig. 4(b). The detailed model is given in Appendix A. For this demonstration, all fiducials are at roughly the same Z-axis height and uses a simplified model which assumes no Z-directional gradients. The error model considers low-order thermal expansion terms; however, machine tools with large strokes (e.g., gantry-framed machine tools) or parts which require long Z-axis travel may have more complex thermal deformations such as sagging and twisting that need to be described by higher-order, and possibly nonlinear, models. In this case, more Fms would be required. Theoretically, the thermal error compensation strategy in this paper can be applied to any machine tool with any size. These models can be directly incorporated into the compensation framework given in this paper.

2.3. Error compensation via G-code modification

A G-code modification method, as illustrated in Fig. 4(c), is utilized to compensate the errors using the inverse kinematics of the error model. In this study, the G-code is modified based on the mirror compensation method, which reduces contouring errors by measuring and then compensating for the TCP drifts using a symmetrical correction [33]. This method is widely applied for machining error compensation, especially for the kinematic errors of five-axis machine tools [34,35]. The actual path differs from the command path due to the thermal drifts. These errors are predicted by the error model, and the compensated command path is found by transforming the original command path through the inverse error model as

$$\begin{bmatrix} x_{comp} & y_{comp} & z_{comp} & 1 \end{bmatrix}^T = \mathbf{M}^{-1} \begin{bmatrix} x_n & y_n & z_n & 1 \end{bmatrix}^T \quad (2)$$

In this case, the compensation is based on the measured thermal drifts. Thus, rapid measurement and short data-processing time are required to achieve the proposed in-process measurement and compensation. The error compensation process in detail is demonstrated in both Animations S1 and S2.

3. Measurement methodology

The measurement methods introduced in [31,32] utilized data-processing algorithms that required a substantial amount of time for video processing [31], pattern recognition [32], and the construction of a fiducial coordinate frame (FCF); therefore, these methods could not be utilized for in-process measurement and compensation. In this study, two methods, denoted Method I and Method II, are introduced to substantially reduce the measurement period, allowing the thermal error measurement and compensation strategy to be conducted "in-process". In Method I, a measurement technique having a low computational cost is used and, in Method II, the data processing with measurement tasks are synchronized. The two measurement methods demonstrate the ability of the proposed compensation strategy to accommodate various measurement techniques. Fig. 5 gives an overview of both methods, which are discussed in detail in Sections 3.1 and 3.2. Section 3.3 compares the time and cost for each method.

3.1. Method I

The procedure is illustrated in Fig. 5(a). First, the pixel length is calibrated by using images of the Fc. Second, due to spindle tolerancing (e.g., spindle taper errors), a slight misalignment between the spindle and microscope will occur each time the microscope is mounted, leading to in-plane deviations as illustrated in Fig. 6, and thus, the location of the spindle rotation centerpoint in the image coordinate frame (ICF) is identified each time the microscope is mounted in the spindle. Further, the orientation between the MCF and the ICF is identified each time the microscope is mounted in the spindle. Finally, thermal drifts are determined where the XY errors are the in-plane deviations projected to the MCF, and the Z errors are the out-of-plane deviations.

3.1.1. Pixel length identification

The pixel length is computed by taking an image of the Fc and measuring features with known lengths. A wireless digital microscope

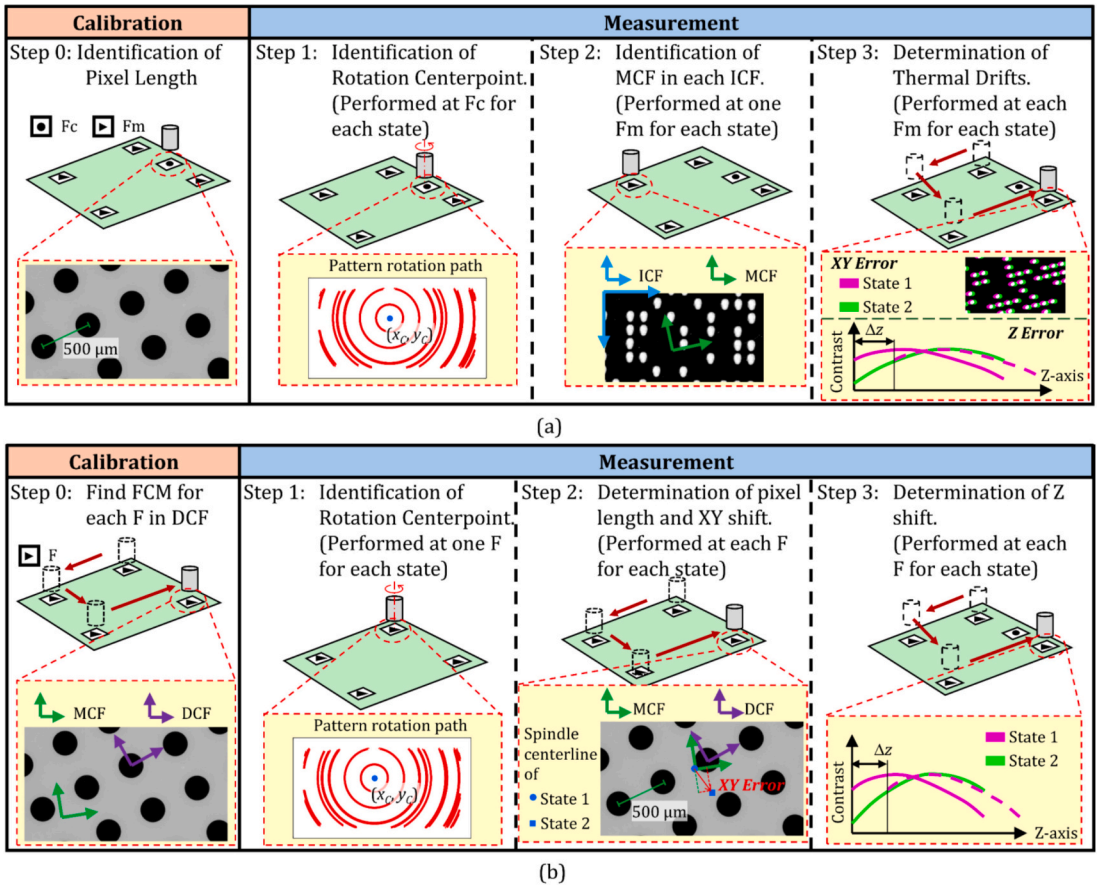

Fig. 5. Measurement procedure overview. (a) In the Calibration phase for Method I, the pixel length is identified though one image of the Calibration Fiducial. The Measurement process follows the procedure of Steps 1–3 to determine three-dimensional thermal drifts of the Measurement Fiducials. States 1 and 2 refer to the machine tool before and after thermal deformation, respectively. (b) The Calibration phase for Method II identifies the machine tool coordinate system relative to the fiducial grid frame. The Measurement process follows the procedure of Steps 1–3 to determine three-dimensional thermal drifts of the Fiducials.

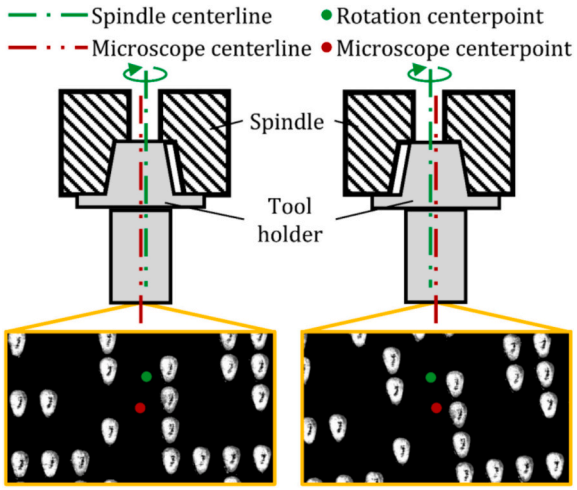

Fig. 6. Schematic of microscope misalignments due to spindle tolerancing and its effects on the microscope view. The microscope centerline is located at the image center constantly, and if the microscope is once dismounted from the spindle, the location of spindle centerline in the image, and the microscope orientation may change as well.

(AmScope DM756AD-W1080, pixel range: 1920 × 1080) is adopted in this attempt and the Part of the Fc is a white ivory distortion target (Edmund Optics 59–210). The measuring feature is the center-to-center distance of 500 ± 2 μm (Type B) dots, as shown in Fig. 7. An LED-ring (3 W and 48 LEDs) is mounted along with the microscope objective lens, as shown in Fig. 7, such that the ambient lighting condition does not affect the microscope view.

The pixel length l_p is

$$l_p = \frac{l}{\frac{1}{N_f}\sum_{i=1}^{N_f} L_i} \tag{3}$$

where l is the nominal distance between neighboring dot centers (i.e., 500 μm), L_i is the measured length of the i^{th} centroid-to-centroid distance in pixels, as labeled in Fig. 7 Callout **1**, and N_f is the number of L_i (i.e., $N_f = 7$ for the demonstration in Fig. 7). Since the dots are in high contrast to the background, the centroid coordinates in the ICF are identified using the regionprops function (MATLAB Image Processing Toolbox or Python Scikit-image Library) directly, with the image binarized to a threshold value of 0.5. The identified pixel length in this method is $l_p = 0.534$ μm.

Additionally, since the microscope resolution is 1 pixel, identification of the centroid-to-centroid distances have an uncertainty of ±0.5 pixel, such that the upper and lower ranges of the identified pixel length,

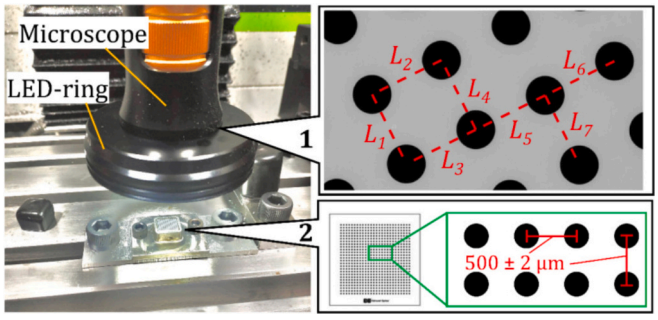

Fig. 7. Pixel length identification using the Calibration Fiducial (Fc). The Callout **1** shows the microscope view where dashed lines indicate the centroid-to-centroid distances of the dots, and the Callout **2** shows the Fc pattern schematic and lengths between dots in a zoom-in view.

respectively, are

$$l_{p,u} = \frac{l + 2\,\mu\text{m}}{-0.5 + \frac{1}{N_f}\sum_{i=1}^{N_f} L_i} \quad l_{p,l} = \frac{l - 2\,\mu\text{m}}{0.5 + \frac{1}{N_f}\sum_{i=1}^{N_f} L_i} \tag{4}$$

In this study, $l_{p,u} = 0.536$ μm and $l_{p,l} = 0.532$ μm; therefore, the actual pixel length is $l_p = 0.534 \pm 0.002$ μm (Type B). Since the Fc is made of soda lime glass (coefficient of thermal expansion, CTE = 9×10^{-6}/K), its deformation due to ambient temperature variations is ignored.

3.1.2. *Identification of rotation centerpoint*

The microscope is mounted in the spindle using a BT-30 tool holder. As mentioned above, the rotation centerpoint is identified every time the microscope is re-mounted in the spindle due to the spindle tolerances. The calibration method for the rotation centerpoint location, discussed in [31], begins with recording a video of one full spindle rotation at the Fc, and locating the dot centroids for each frame of the video using the regionprops function. Through tracking the centroid path of the dots, the rotation centerpoint location in the ICF is calibrated by fitting all the paths to concentric arcs of the center of rotation using least-square method [31], as shown in Fig. 8(a).

To investigate the uncertainty of the rotation centerpoint identification, 10 videos were recorded at 25 fps (frames per second). In each video, the spindle completed one rotation in approximately 10 s. The spindle was rotated manually, because the motor's minimal rotation speed for the utilized machine is too fast. To minimize potential manual-

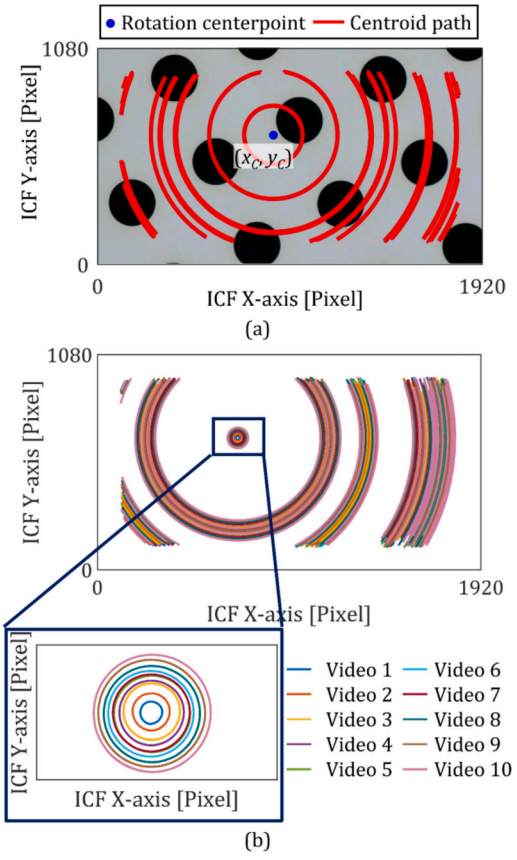

Fig. 8. (a) illustration of the tracked dot centroid paths from each video to identify the rotation centerpoint (x_C, y_C) in the image coordinate frame (ICF) and (b) tracked paths of ten videos where the microscope slightly moved in the XY plane in the machine coordinate frame (MCF) but was not dismounted from the spindle (i.e., no spindle tolerance effects). From the zoom-in view of (b), it can be observed that the paths are not purely concentric circles, such that an uncertainty in the rotation centerpoint location exists.

induced errors (e.g., vibration, asymmetric loading), the torque was applied to the tool holder exclusively, ensuring no direct contact with the microscope body. The tracked dot centroid paths are shown in Fig. 8 (b). The expanded uncertainties in the rotation centerpoint identification are ±1.4 and ± 0.8 pixels (Type A, $k = 2$, where k represents the uncertainty coverage factor, i.e., the number of standard deviations contained within the reported confidence interval) in the ICF X and Y-directions, respectively. The uncertainty is due to both the algorithm and the inherent rotational accuracy of the machine tool spindle.

3.1.3. Identification of MCF orientation

The orientation of the MCF's XY plane in the ICF is identified by taking images with the spindle moving along the X- and Y-axes relative to the worktable and tracking the motions of patterns on the Fm. The displacements among the images are recognized similarly to the in-plane deviation, as shown in Fig. 2(b), such that this step is conducted using Fm.

The Fms in this method are self-fabricated parts with evenly distributed but non-periodic patterns (see Fig. 9), which are laser engraved on black-painted aluminum using a ComMarker LLC B4—60W laser engraver. Aluminum has a CTE of 25×10^{-6}/K; therefore, even if the temperature increases by 40 °C, a 1-mm region imaged under the microscope only expands by 1 μm, i.e., the microscope view is zoomed-in by 0.1%. This distortion can be neglected. Also, the fiducials are very small compared to the worktable surface to which they are attached, and the fiducial is symmetric, thus, their thermal deformation can be ignored.

A phase-based two dimensional Fast Fourier Transformation (2D-FFT) algorithm [36] is used to calculate the image translation. These methods are commonly utilized to determine the shifts between two images that translate relative to one another. The algorithm is described in detail Appendix B.

$$\mathbf{v}_i = \frac{\begin{bmatrix} \Delta p_{xi} & \Delta p_{yi} \end{bmatrix}}{\left\| \begin{bmatrix} \Delta p_{xi} & \Delta p_{yi} \end{bmatrix} \right\|} \quad (i = 1 \sim N_v - 1) \tag{5}$$

where $\begin{bmatrix} \Delta p_{xi} & \Delta p_{yi} \end{bmatrix}$ is the identified displacement in pixel using 2D-FFT algorithm, and the orientation of the MCF in the ICF is

$$\mathbf{v}_\xi = \frac{1}{N_v - 1} \sum_{i=1}^{N_v - 1} \mathbf{v}_i \quad (\xi = X, Y) \tag{6}$$

3.1.4. Determination of thermal drifts

The in-plane deviations, shown in Fig. 2(b), are determined the 2D-FFT algorithm given in Appendix B. However, the spindle tolerances (see Fig. 6) cause variations of the rotation centerpoint location in the microscope view and the orientation of the microscope view. For CNC machine tools without spindle rotary encoders, the second variation is common.

To address these issues, the rotation centerpoint location is calibrated every time the microscope is remounted in the spindle, as mentioned in Section 3.1.2. Further, the angular deviation between images is modified such that the two images have the same orientation.

The angular deviation between two images is modified by aligning the orientation of State 2 to State 1. A demonstration is shown in Fig. 10, where Fig. 10(a) and (b), denoted as $\mathbf{f}^{(1)}$ and $\mathbf{f}^{(2)}$, are the images captured in the two states (the angular deviation between $\mathbf{f}^{(1)}$ and $\mathbf{f}^{(2)}$ here is made intentionally). To align the orientation, a new image, $\mathbf{f}_r^{(2)}$, is constructed for Fig. 10(b), as shown in Fig. 10(c), where a black image, i.e., $\mathbf{f}_r^{(2)} = \mathbf{0}_{M \times N}$, is defined firstly, and then constructed by

$$\mathbf{f}_r^{(2)}\left(p_{xr}, p_{yr}\right) = \mathbf{f}^{(2)}\left(p_x, p_y\right), \ \forall 1 \le p_{xr} \le M, 1 \le p_{yr} \le N \tag{7}$$

where

$$\begin{bmatrix} p_{xr} \\ p_{yr} \end{bmatrix} = \text{round}\left(\begin{bmatrix} \cos(-\Delta\theta) & -\sin(-\Delta\theta) \\ \sin(-\Delta\theta) & \cos(-\Delta\theta) \end{bmatrix} \begin{bmatrix} p_x - x_C^{(2)} \\ p_y - y_C^{(2)} \end{bmatrix} + \begin{bmatrix} x_C^{(2)} \\ y_C^{(2)} \end{bmatrix} \right) \ \forall \mathbf{f}^{(2)}\left(p_x, p_y\right) \neq 0 \tag{8}$$

Suppose a total of N_v images are taken to identify the orientation of the MCF X- or Y-axis, the unit vector in the direction of motion from the i^{th} to the $(i+1)^{\text{th}}$ image is

and $\begin{bmatrix} x_C^{(2)} & y_C^{(2)} \end{bmatrix}$ denotes the rotation centerpoint (shown in Fig. 10) whose superscript corresponds the thermal state, and $\Delta\theta$ is the angular

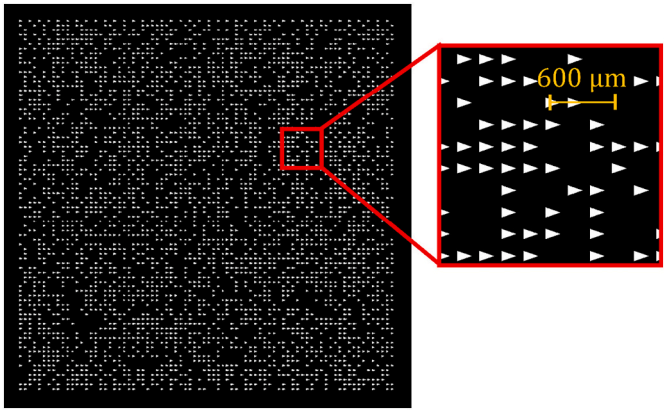

Fig. 9. Measurement fiducial schematic with zoomed-in area. The pattern is a triangle grid whose bottom and height are 80 μm and 150 μm, respectively, and the centroid distance is 200 μm. A Sobol-random algorithm is applied to generate a binary matrix, which indicates the triangle shape printed or not on the grid, to make a non-periodic pattern with low discrepancy.

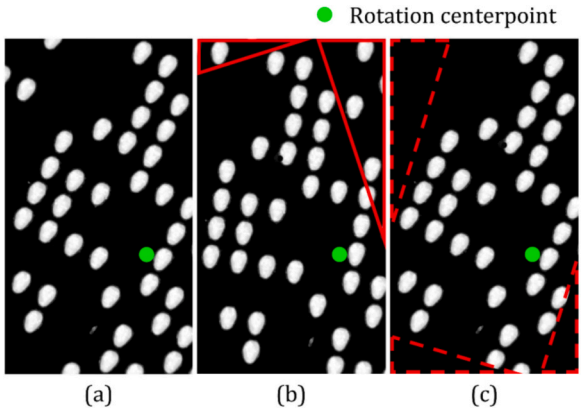

Fig. 10. Images for XY-axis error measurement in the machine coordinate frame. (a) $\mathbf{f}^{(1)}$, (b) $\mathbf{f}^{(2)}$, and (c) $\mathbf{f}_r^{(2)}$. Pixels in solid-line areas in (b) leave image in (c) and dashed-line areas in (c) are unknown pixels rotated into the image and set to zero. After the modification, (a) and (c) are in the same orientation.

deviation between the images. Since the fiducials do not dismount from the worktable, $\Delta\theta$ are determined as the angular deviations between the orientations of corresponding MCFs

$$\Delta\theta = \text{sign}\left(\mathbf{v}_X^{(2)} \bullet \mathbf{v}_Y^{(1)}\right) \bullet \left(\arccos\left(\mathbf{v}_X^{(1)} \bullet \mathbf{v}_X^{(2)}\right) + \arccos\left(\mathbf{v}_Y^{(1)} \bullet \mathbf{v}_Y^{(2)}\right)\right)/2 \tag{9}$$

Essentially, the matrix $\mathbf{f}_r^{(2)}$ is populated by rotating the original image by $\Delta\theta$ and discarding the pixels that rotated out of the image, e.g., the green areas in Fig. 10(b), and assigning zeros to pixels rotated into the image, e.g., the red areas in Fig. 10(c). Practically, the rotation between the two images is small in the sense that enough pixels of the original image can be recovered and utilized to accurately determine the in-plane deviations. In this case, the in-plane deviations are

$$[\,\Delta x_I \quad \Delta y_I\,] = \left(\mathbf{e}_I - [\,x_C^{(2)} - x_C^{(1)} \quad y_C^{(2)} - y_C^{(1)}\,]\right) \tag{10}$$

where $\mathbf{e}_I$ represents the in-plane deviations between Fig. 10(a) and (c), determined by the 2D-FFT algorithm.

The out-of-plane deviation is determined using the contrast-based method given in [32]. A contrast value, determined using the Gaussian derivative method [37], is utilized to determine the image focal distance. Five images with different focal distances (created by adjusting machine tool Z-axis displacement) are captured for each measurement, and a contrast metric curve, $\mathbf{\Psi}^{(i)}(z) \quad (i = 1, 2)$, is created. The out-of-plane deviations between States 1 and 2 are determined by aligning the contrast metric curves, as shown in Fig. 11. The detailed algorithm is given in Appendix C. From Fig. 11, it can be seen that the initial position of the microscope needs to be close to the in-focus position (i.e., where the contrast value is maximal) to ensure that the out-of-plane deviations can be measured in both directions.

According to the algorithms in Appendices B and C, the measurement ranges of in-plane and out-of-plane measurements are theoretically equal to the image size in pixels and the Z-axis displacement conducted in the measurement process, respectively. The detailed procedure of Method-I is demonstrated in Animation S1.

3.2. Method II

In this method, the measurements were performed with a STPCTOU PF018005 1080p wireless digital microscope. This microscope is equipped with eight LED lights to provide consistent illumination. Four high-precision fiducials (Fc in Method-I) were used for both calibration and measurement (i.e., Fc and Fm are the same fiducial, and thus, they are referred to as F1 ~ F4). The thermal drifts are measured based on the methods proposed by Vogl et al. [31]. Compared with Method I, Method II uses the same general algorithms for pixel length calibration, rotation centerpoint identification, and contrast-curve shift. However, instead of using the 2D FFT algorithm to calculate the XY displacement, the in-plane deviations are determined by analyzing how the dot grid has shifted relative to the rotation centerpoint location. The orientation of the MCF relative to the dot-grid coordinate frame (DCF) is pre-calibrated when the fiducials are installed on the machine. Displacements are calculated relative to the DCF and then converted to the MCF. This removes the need to measure the MCF every time the microscope is installed in the spindle provided the microscope angle changes by less than 45 degrees, which is easily accomplished for machine tools equipped with a spindle rotation encoder. See Section 5.3 for a full uncertainty analysis for the Method II measurement and compensation system.

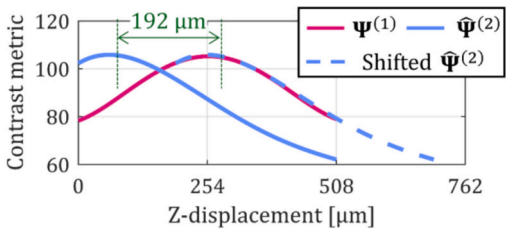

Fig. 11. Demonstration of the out-of-plane deviation. The curve $\hat{\mathbf{\Psi}}^{(2)}$ is shifted 192 μm along Z-displacement in this case, aligning it with $\mathbf{\Psi}^{(1)}$; therefore, the out-of-plane deviation is 192 μm.

3.2.1. Modifications on algorithms and implementation

In this study, several modifications to [31] are made to improve measurement, data processing speeds, and measurement accuracy. First, the rotation centerpoint location in the ICF is identified only on F1 rather than all four fiducials, and this location is then applied to still images taken over F2 ~ F4 to identify the image shifts. Since this removes three recorded videos of rotation compared with [31], it saves a significant amount of measurement time from each cycle.

Second, the spindle rotation speed during the measurement is increased from 3 to 20 rpm. Since each rotation measurement requires a full spindle rotation, this reduces measurement time by 17 s. The influence of this increased rotation speed on the measurement uncertainty is discussed in Section 5.3.

Third, a phase-coding Hough transform algorithm is employed to track the circular targets [38]. Hough transforms are widely used in image processing due to their computational efficiency and robustness against image noise and occlusion. Instead of finding the circle center as the centroid of the individual pixels, the Hough transform identifies edges in the image using the brightness gradient. Each edge pixel casts "votes" for each possible circle they could belong to in an equation-space accumulator matrix. The peaks of this accumulator represent the fit circles in the image. The circle centers identified with the Hough transform are effectively identical to the previous regionprops method (changes are <0.5 pixels), but the new method is more than three times faster. This was further improved by introducing multithreading and general code optimization. The identified circles are tracked through the video under the assumption that each circle will move less than 50 pixels between frames. Circles which do not have any match within that distance tolerance are assumed to be new dots entering the image. This is problematic for circles which are farther away from the rotation centerpoint since they may be moving faster than that 50 pixel per frame threshold. This can result in gaps in the tracked sequence; see the video at Animation S2 for an example.

Therefore, the fourth improvement was implementing a two-step weighted least-squares algorithm to find the center of rotation. The first step uses the same least-squares algorithm described in [31], where x_q^p, y_q^p are the p^{th} observed points belonging to the q^{th} tracked dot, R_q is the radius of the circle for the q^{th} tracked dot, and x_c, y_c are the fit centerpoint which all tracked dots are rotating around. This is shown in Eq. (11).

$$\begin{bmatrix} -2x_1^1 & -2y_1^1 & 1 & 0 & \\ -2x_1^2 & -2y_1^2 & 1 & 0 & \\ & & \vdots & & \cdots \\ -2x_2^1 & -2y_2^1 & 0 & 1 & \\ & & \vdots & & \end{bmatrix} \begin{bmatrix} x_C \\ y_c \\ x_c^2 + y_c^2 - (R_1)^2 \\ x_c^2 + y_c^2 - (R_2)^2 \\ \vdots \end{bmatrix} = \begin{bmatrix} -\left(x_1^1\right)^2 - \left(y_1^1\right)^2 \\ -\left(x_1^2\right)^2 - \left(y_1^2\right)^2 \\ \vdots \\ -\left(x_2^1\right) - \left(y_2^1\right)^2 \\ \vdots \end{bmatrix} \tag{11}$$

After this first iteration, each observation is then weighted by the inverse of its fit radius, giving the weights $w_q = 1/R_Q$. These weighted observations are then used to fit a new center of rotation using Eq. (12). This gives higher weight to points which are closer to the center of rotation, which gives improved accuracy since it reduces the impact of dots close to the edge of the image which are not tracked for an entire revolution or which may be moving too fast to accurately track from frame to frame.

$$\begin{bmatrix} -2x_1^1 w_1 & -2y_1^1 w_1 & w_1 & 0 & \\ -2x_1^2 w_1 & -2y_1^2 w_1 & w_1 & 0 & \\ & & \vdots & & \cdots \\ -2x_2^1 w_2 & -2y_2^1 w_2 & 0 & w_2 & \\ & & \vdots & & \end{bmatrix} \begin{bmatrix} x_C \\ y_c \\ x_c^2 + y_c^2 - (R_1)^2 \\ x_c^2 + y_c^2 - (R_2)^2 \\ \vdots \end{bmatrix}$$

$$= \begin{bmatrix} w_1\left(-(x_1^1)^2 - (y_1^1)^2 \right) \\ w_1\left(-(x_1^2)^2 - (y_1^2)^2 \right) \\ \vdots \\ w_2\left(-(x_2^1) - (y_2^1)^2 \right) \\ \vdots \end{bmatrix} \quad (12)$$

3.2.2. Automation framework

A framework was built to automatically process incoming videos as they are saved, rather than waiting for the full measurement cycle to conclude before starting the analysis. This framework is illustrated in Fig. 12. There are three separate components to the framework. The machine tool moves the microscope between the different measurement locations to measure each fiducial. LabVIEW communicates with the microscope and saves the microscope video. MATLAB analyzes the videos to calculate the thermal drift. Once all the required measurements have been performed, MATLAB then generates a compensated G-code program, along with a set of diagnostics to help the operator confirm the validity of the measurements.

Communication between the machine tool and LabVIEW is based on the contrast of the microscope video. To start recording a video, the machine rotates the spindle at 300 rpm for one second, which causes a sharp drop in contrast as the video blurs (see Animation S2). When LabVIEW detects this drop in the video contrast, it begins saving the microscope images to a new measurement folder for analysis. This allows the measurement process to be automated without requiring direct communication with the machine tool controller, which reduces deployment complexity.

Uncertainty analysis of this method is experimentally investigated as well, and the details are introduced in Section 5.3.

3.3. Comparison of timing requirements

The comparison of timing requirements for each measurement method is shown in Table 1. The top section of the table shows the isolated measurement and calculation time required over each fiducial for each individual component of the measurement, omitting any time required for the machine to translate between the different fiducials. The bottom section of the table shows the total time required to conduct the measurement cycles used in the experimental validation described in Sections 4 & 5, measured from the moment the measurement is begun to the moment the data analysis is complete. Through the comparison, it can be seen that the methods proposed in this study significantly reduced the total measurement timing requirements, such that the measured thermal drifts can be used for in-process compensation. Note that Methods I and II were demonstrated using different machine tools and computers (detailed in the footnotes of Table 1) and thus, the data given in Table 1 are not being compared. Rather, the data indicate the operational feasibility of both methods for in-process thermal compensation.

Comparing the two methods in this study, the 2D FFT algorithm performs faster in image analysis when determining the XY-errors. However, Method II behaves much faster since a) the excellent

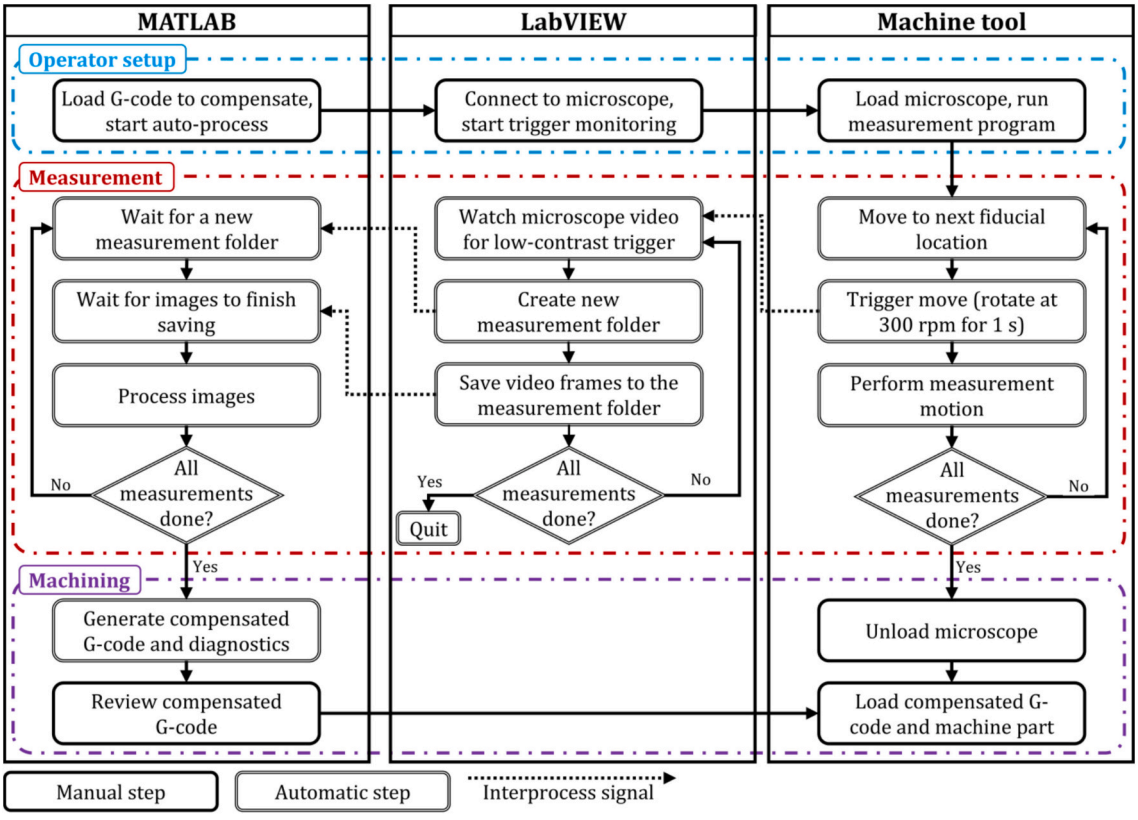

Fig. 12. Flowchart illustrating the auto processing framework used for Method II. The machine tool runs the measurement G-code program and moves the microscope to each measurement location. LabVIEW monitors the incoming microscope video and saves the microscope video to a measurement folder when a trigger is observed. MATLAB processes images added to the measurement folders. When measurements are done, MATLAB automatically generates a new compensated G-code machining program, which the user can load onto the machine tool and run.

Table 1
Timing requirements for measurement methods.

Measurement step		Vogl et al. [31]	Li et al. [32]	M-I[a]	M-II[b]
Single fiducial measurement time					
Pixel length identification		Contained in other measurement steps			
Rotation centerpoint	MEA[c]	12	10	10[e]	6[e]
	DP[d]	18	70	30[e]	2.5[e]
MCF orientation	MEA	12	10	10	(-)
	DP	20	70	1.2	(-)
XY-error determination	MEA	(-)	(-)	1	2
	DP	1	70	0.2	0.6
Z-error determination	MEA	16	10	10	9
	DP	22	0.5	0.5	0.9
Time for measurement in experimental studies[f]					
Total measurement-and-calculation time for four fiducials		448	272	98.2	85

(-) Contained in other measurement steps;
[a] Method I, calculated on a desktop computer (Intel i5-13400F).
[b] Method II, calculated on a laptop (Intel i9-13950HX).
[c] MEA: measurement process.
[d] DP: data-processing process.
[e] Only required on one fiducial per thermal state.
[f] Total time required to perform a full measurement of four fiducials on a machine tool, including all machine motion, measurement, and data processing. For M-I and M-II, this is based on the studies described in Sections 4 and 5, respectively: see videos uploaded along with this paper. These experiments were performed on different machines and may not be directly comparable.

performance of Hough transform algorithm in rotation centerpoint identification and b) the angle between DCF and MCF is pre-calibrated and does not need to be measured during the main cycle. Since the actual microscope measurements and machine motion currently dominate the data collection, Method II is the fastest among all the methods. However, only one high-precision fiducial (list price of $710 each as of writing [39]) is used in Method I, which significantly reduces the up-front costs.

4. Experimental study using Method I

A three-axis machine tool (Tormach 1100 MX, X/Y/Z travels: 457/279/413 mm, axis resolution: 2.54 μm) is utilized for the experimental study described in this section. One Fc and four Fms are placed on the worktable, and the arrangement is shown in Fig. 3(d). In one measurement routine, the microscope moves to the Fc first to identify the pixel length and rotation centerpoint. The microscope subsequently moves to Fm1 to determine the MCF orientation and then travels from Fm1 to Fm4 to collect measurements. When the measurement is finished, the microscope is removed from the spindle while the fiducials remain on the worktable. When the machine tool is thermally deformed (e.g., after a long period of machining process or ambient temperature changes a lot), the microscope is remounted to the spindle and repeats the measurement routine, such that the thermal drifts are measured.

4.1. Microscope thermal deformations

The microscope must reach thermal equilibrium before measurement to minimize the uncertainties due to the movement of optical components from microscope structural deformations. A test was conducted to investigate the length of time required to sufficiently warm up the microscope used in this study. The microscope, fixed at the calibration fiducial as seen in Fig. 7, was powered on and then acquired images at a rate of 1 fps. Computing the displacements in the ICF between the initial and subsequent images and contrast values, the errors arising from the microscope warmup process are shown in Fig. 13.

According to the result, the time for the microscope to achieve

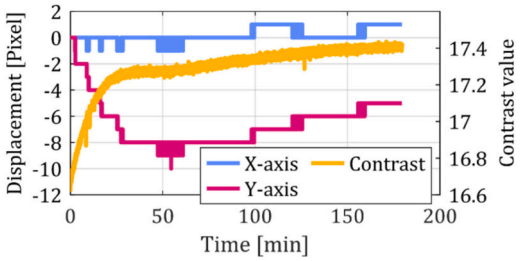

Fig. 13. Displacements in the image coordinate frame (ICF) and contrast value variation due to the microscope warmup process. The machine tool axes are not moved during these measurements; therefore, the measured shifts are due solely to changes in the camera thermal state. The microscope achieves thermal equilibrium after approximately 30 min.

thermal equilibrium is approximately 30 min. However, after 1 h the Y-axis displaced an additional 1.5 μm, and contrast value changed around 0.2, which will be seen to be less than the total measurement uncertainty. These displacements are possibly due to changes in the ambient temperature (e.g., the air conditioning unit turned on/off). If the microscope encounters thermal loads between measurements, the induced errors will directly affect the measurement errors. In this case, either these errors are taken as a component of the measurement uncertainty, or these errors are determined by measuring a thermally isolated fiducial. For the X and Y axes, these ICF displacements are not critical since displacements are calculated relative to the center of rotation, which is identified before every measurement. Therefore, the X and Y axis measurements are only affected by the microscope drift over the course of one measurement. However, the Z axis measurements are directly affected by the contrast change. The contrast value shift of 0.7 experienced over the course of one hour corresponds to approximately a 5-μm shift in the Z-axis position; therefore, the microscope is warmed up before taking measurements. In this study, all measurements were taken after the microscope was warmed up for one hour and remained powered throughout the entire measurement process.

Thermal deformation of the microscope holder may cause measurement uncertainty as well. For manufacturing environments where the ambient temperature substantially changes, this potential error source can be mitigated by temperature control of the measurement device. Long microscope warm up tests (in the previous studies) demonstrated that the ambient temperature change during the measurements conducted in this paper did not affect the resulting measurements. Machine tool vibrations may also affect the microscope measurements; however, this can be prevented by ensuring the machine tool is stationary when the measurements are taken.

4.2. Repeatability at machine tool cold state

A measurement repeatability test was conducted where the measurement routine was repeated six times while the machine tool was in the cold state, i.e., the machine tool only operates to take measurements, such that thermal deformations do not occur. Further, the microscope was removed from the spindle and mounted again for each measurement. The errors between the later five measurements and an initial measurement were calculated for all four fiducials. During these measurements, four K-type thermocouples, denoted TC1 ~ 4, are used to monitor temperature variations: TC1 (worktable top surface near Fm3 and not shown in Fig. 14(a)), TC2 (near the X-axis motor housing), TC3 (spindle housing), and TC4 (on a wall far from the machine tool). The locations of the thermocouples are schematized in Fig. 14(a). The temperature variance during the repeatability test is shown in Fig. 14(b). It can be seen that the X-axis motor temperature slightly increased (temperature variation of T2 is 0.5 °C), while the others remained nearly constant. These results show that convection from the air currents do not affect the thermal stability of the fiducials.

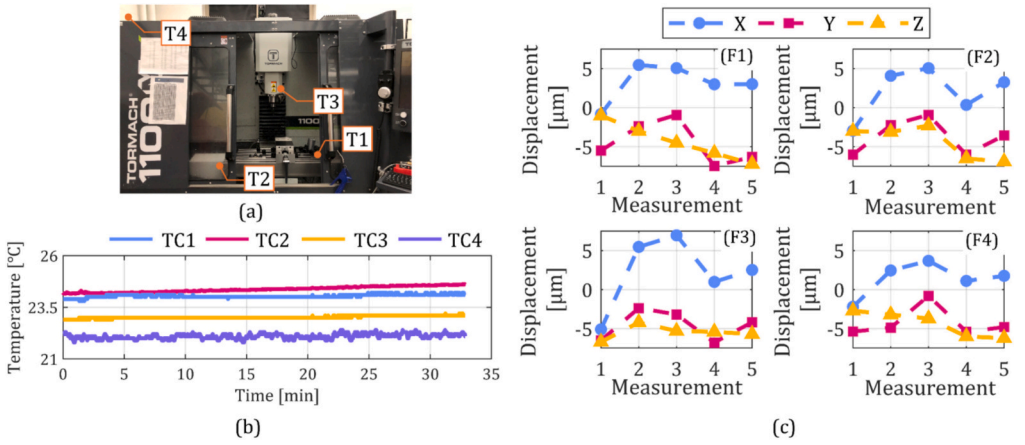

Fig. 14. Placement of thermocouples and measurement results of repeatability tests. (a) schematizes the placements of TC1–4; (b) shows the temperature variation during the repeatability tests; (c) shows the measured drifts of each fiducial.

The measurement results are shown in Fig. 14(c). The maximum absolute deviation from the zero-reference for all three axes is within 7.3 μm (i.e., approximately three times the machine tool resolution). Consequently, the maximum peak-to-peak variation across the measurements reaches approximately 12.3 μm (i.e., approximately five times the machine tool resolution). The expanded measurement uncertainty for a single microscope measurement was calculated based on the standard deviation for the data across all three axes as 7.9 μm ($k = 2$). Since measuring thermal drifts involves comparing two uncorrelated microscope measurements, the expanded uncertainty is therefore $7.8\sqrt{2} = 11.2$ μm ($k = 2$). This uncertainty estimate consists of both uncertainty inherent to the Method I microscope/data analysis and uncertainty due to the machine tool positioning repeatability and thermal drift over the half hour measurement period. Therefore, this value should be considered as the overall measurement/compensation expanded uncertainty for the Method I experimental study described in this section and represents an upper bound for the inherent uncertainty of the Method I measurement.

4.3. In-process measurement and compensation

4.3.1. Thermal drift measurement

The ISO 10791-7 M1 specimen [40], here denoted ISO specimen, was adopted in the experimental study. The material is Aluminum 6061-T6 and its dimensions were reduced proportionally to a 99.06 mm × 99.06 mm square to fit the machine tool workspace, as shown in Fig. 15. Three sets of experimental studies (denoted E-I, E-II, and E-III) were conducted. The experimental procedures are shown in Fig. 16. The warmup process involves moving the X and Y axes back and forth for 165 min along a diagonal line of 466.3 mm in length through the workspace at the machine tool's maximum feed rate (8842 mm/min).

As seen in Fig. 16, for each experiment, State 1 is the set of measurements taken in the machine tool's cold state, i.e., before any axis or spindle motions, and State 2 is the set of measurements taken after the rough cut (E-I) or warmup procedure (E-II and E-III). This process uses the warmup procedure to induce a thermal load in between machining the part datums and the measurement features. Therefore, errors in the relative positions of the machined datums and measurement features between the E-I and E-II experiments reflect thermal distortion in the machine tool, while the proposed compensation method should result in the E-III case more closely resembling the E-I case. The microscope was warmed up for more than 1 h to ensure it was in thermal equilibrium before taking measurement of State 1 and remained powered until measurement of State 2 was finished. It will not deform due to the heat from the spindle since it is only mounted in the spindle for short periods of time during the measurement process as seen in Table 1. A pre-

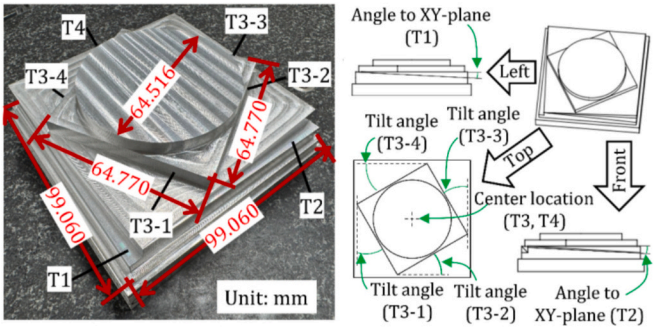

Fig. 15. ISO specimen machined in the experimental study. Dimensions (unit: mm) are proportionally reduced compared with the original design. T1–T4 indicates Measured features, where T1 and T2 are slopes whose normal vector direction variation is due to the machining errors of the machine coordinate frame (MCF) Z-axis, T3 is a tilted square shape whose tilt angle variation of its four sides are affected by the thermal-induced errors along the MCF X- and Y-axes, and T4 is a circular shape whose radius is affected by the thermal-induced errors along the MCF X- and Y-axes. The center location variations of Features T3 and T4 are affected by the thermal-induced errors along the MCF X- and Y-axis.

measurement was implemented to record the temperature variation of the warmup process without machining, as shown in Fig. 17(a). It can be seen that significant heat was generated from the motors while the ambient, spindle, and worktable temperatures had only slight variations. Therefore, temperature variations of the microscope holder and fiducials due to the warmup process can be ignored. During the warm-up processes of E-II and E-III, the ambient temperature was recorded, as shown in Fig. 17(b). It can be seen that the ambient temperature varied less than 1 °C. The other thermocouples were not utilized in the machining tests since they would be flushed away by the coolant Given the measurement of the ambient temperature and the previous temperature results, it is assumed that the microscope and fiducials did not significantly deform during E-II and E-III.

The thermal drifts between States 1 and 2 at each Fm for all three tests are shown in Fig. 17(c). The drifts for E-I are all within the measurement uncertainty; therefore, these errors are too small to clearly distinguish their main root cause, whether thermal or non-thermal deformed.

In contrast, the warmup process caused large thermal deformations at all four fiducials compared with E-I, as seen in Fig. 17(c). The drifts presented in E-II are similar to those in E-III since the warmup procedure is the same for both experiments. For the drifts along the X-axis, the

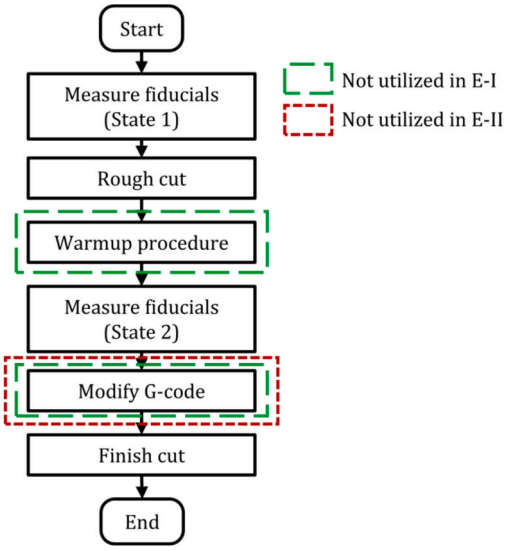

Fig. 16. Experimental procedure flowchart. Machine warm-up procedure is only used for E-II and E-III, and G-code is only modified for thermal error compensation in E-III. Hence, States 1 and 2 represent the measurements before and after, respectively, the machine tool thermally deformed.

drifts measured at F3 and F4 are more than 30 μm larger than those measured at F1 and F2. The reason is that the X-axis motor, which is a major heat source in this experiment, causes X-axis thermal expansion that affects X-axis positions that are farther from the motor, such as F3 and F4 that are approximately 350 mm farther from the motor than F1 and F2. For drifts along the Y-axis, all fiducials have similar drifts (approximately 20 μm to 30 μm) because the differences in their Y-coordinates are only approximately 60 mm; that is, the Y-axis drifts for F1 to F4 are similar since the Y-axis positions are affected by similar Y-axis thermal expansions. The thermal drifts along the Z-axis direction are similar for all fiducials, approximately 10 μm, which is within the expanded measurement uncertainty. Although the thermal drift at Fm3 is approximately 5-μm larger than those at the other three fiducials, these differences are within the expanded measurement uncertainty. Even though the Z-axis was not run during the warmup procedure, the worktable still expanded thermally in this direction due to the thermal loads from the X and Y motors.

4.3.2. Error model construction

Every time the Fms are measured, a thermal error model is constructed. Therefore, two separate error models are constructed using the measured drifts from E-II and E-III. The parameters for both models are given in Table 2. Since both experiments underwent the same warmup procedure, the measured drifts were very similar. Therefore, the corresponding model parameters are similar. The two notable differences are ΔE_C, which is 5.77 times larger for the E-III model than the E-II model, and ΔE_{XOY}, which is 6.68 times larger in magnitude for the E-III model than the E-II model and has a different sign. While these relative shifts appear large, in an absolute sense they reflect small shifts in the actual measurements over each fiducial which lie within the measurement uncertainty. For example, all four measurement fiducials span a total Y axis travel of roughly 60 mm. The ΔE_{XOY} shift from −7.97 μrad to 53.2 μrad therefore only reflects a total X displacement of 3.7 μm over that measurement span, which is within the expected values based on the measurement uncertainty.

Using the error model, spatial thermal error maps of the worktable using data from E-II and E-III are constructed and compared, as shown in Fig. 18. The Z-axis errors were very similar, i.e., within the measurement uncertainty, while different patterns of X- and Y-axis errors were obtained from E-II and E-III. According to Fig. 18, the ranges of the differences in the X- and Y-axis errors between the two models are [−10, 8] μm and [−19, 6] μm, respectively. Since these differences are larger than the measurement uncertainty, it can be concluded that they reflect real differences in the thermal drift, even though the same warmup was conducted for both experiments. This shows the necessity of the in-process measurement even when the same process plan is followed.

Next, the impact of the different error parameters on the TCPs are

Table 2
Thermal error model parameters.

Error parameter	Identification	
	E-II	E-III
ΔE_X [μm]	11.9	9.83
ΔE_Y [μm]	35.5	36.8
ΔE_Z [μm]	−6.13	−6.67
ΔE_A [μrad]	10.8	30.5
ΔE_B [μrad]	15.6	10.7
ΔE_C [μrad]	−4.44	−25.6
ΔE_{XOY} [μrad]	−7.97	53.2
$\Delta\alpha_X$ [μm/mm]	0.114	0.103
$\Delta\alpha_Y$ [μm/mm]	0.081	0.024

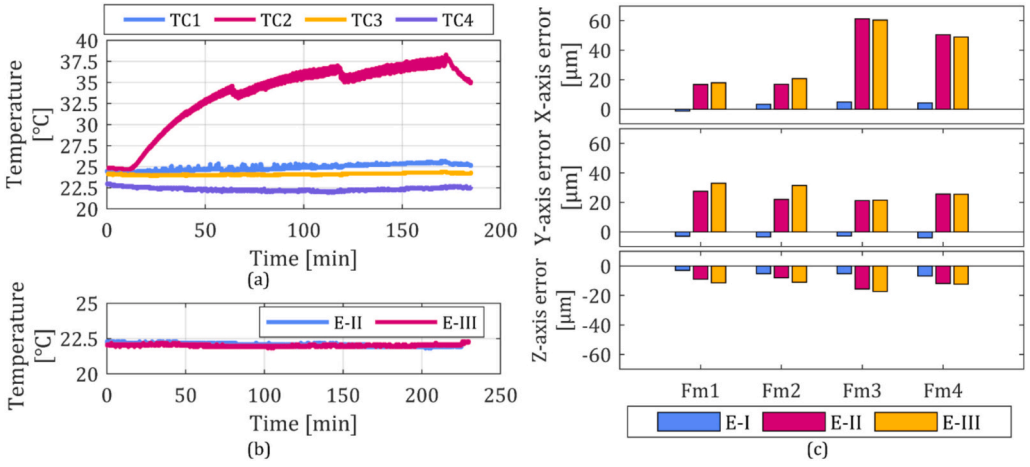

Fig. 17. Results of thermal drift measurement. (a) shows the temperature variation during the warm-up process; (b) shows the ambient temperature variations during E-II and E-III, demonstrating that both tests were conducted under the same ambient thermal states (there is no machine warmup implemented in E-I); and (c) shows the measured thermal drifts for all four Fms in the machine coordinate frame (MCF) (the subplots are in different vertical ranges but have the same scales). Note there was no compensation implemented during these tests.

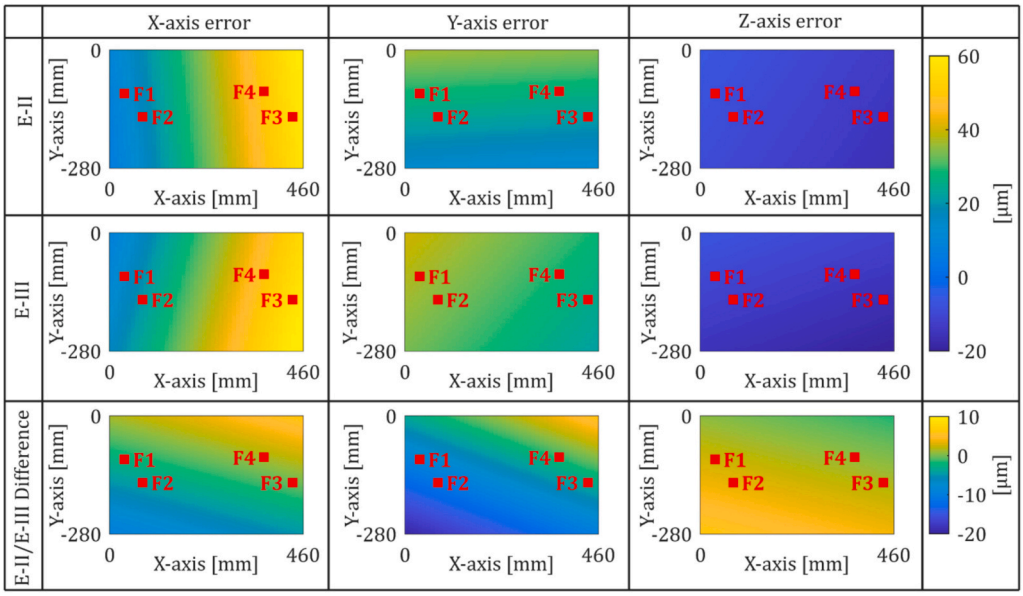

Fig. 18. Predicted drifts in machine coordinate frame (MCF) using the error models determined using the measured drifts of E-II and E-III. The different patterns are mainly due to large differences of ΔE_C and ΔE_{X0Y}.

analyzed to determine which are the most significant. Reducing Eq. (A.1) to the dominant terms, the thermal drifts for a certain TCP in the MCF are

$$\begin{aligned} e_x &= \Delta E_X + \Delta\alpha_X x_n - (\Delta E_C + \Delta E_{X0Y}) y_n \\ e_y &= \Delta E_Y + \Delta\alpha_Y y_n + \Delta E_C x_n \\ e_z &= \Delta E_Z - \Delta E_B x_n + \Delta E_A y_n \end{aligned} \tag{13}$$

where e_x, e_y, and e_z are the thermal drifts along the MCF X-, Y-, and Z-axes, respectively. Eq. (13) indicates that each of the static and first-order terms is significant, and the errors are not a function of z_n, which is due to the fact that all data was gathered at one MCF Z-position, which is z_n = -108 mm. The difference in the X-axis errors between the models obtained from E-II and E-III is mainly in the Y-direction since the signs of $(\Delta E_C + \Delta E_{X0Y})$ are different. The difference in the Y-axis errors is strong in both the X- and Y-directions, respectively, since ΔE_C is an order of magnitude different between the models and $\Delta\alpha_Y$ is different by a factor of four between the models. The difference in the Z-axis errors is mainly in the Y-direction since the difference in ΔE_A is four times the difference in ΔE_B. The differences in parameters between the error models can be traced to differences in the fiducial measurements used to compute the parameters in Eq. (A.3). The condition number of the matrix **S** in Eq. (A.2) is 279, indicating it is sensitive to measurement noise, which can be reduced by the use of more fiducials and the optimization of their locations. Nevertheless, the thermal compensation strategy focuses on the resulting TCP position instead of the real machine physical structure and will be shown to provide excellent compensation in studies with experimental artifacts even when only four fiducials are used.

4.3.3. Compensation results

In this subsection, the thermal-induced workpiece errors after finishing are investigated. Four workpiece features, denoted T1, T2, T3, and T4, are measured (see Fig. 15). Features T1 and T2 were measured with a contact-type surface profile measurement device (Kosaka Laboratory DSF900) with a measurement uncertainty of 1.2 μm (Type B k = 2), and Features T3 and T4 were measured with a contact-type coordinate measuring machine (CMM) system (Mitutoyo CRYSTA-Apex V574) with a measurement uncertainty of 2.1 μm (Type B k = 2). The measurement results are shown in Table 3. Since the Z-positions of the four fiducials were arranged at nearly the same height, the compensation in E-III is essentially a 2.5-dimensional compensation, i.e., XY-planar around a constant Z-axis position.

Table 3
Workpiece quality measurements.

Feature			Deviations to E-I	
			E-II	E-III
Angle to XY-plane [μrad]	T1		91.6	−11.2
	T2		91.8	−37.5
T3 tilt angle [μrad]	1		162	−20.9
	2		117	24.4
	3		−244	−43.6
	4		−54.1	15.7
Center location [μm]	T3	X	56.7	−6.3
		Y	−2.3	2.2
	T4	X	56.5	−0.1
		Y	9.4	0.5

The errors measured on workpiece E-I were found to be within the thermal drift measurement uncertainty and, thus, the machine's thermal state changed very little during its operation. In Table 3, the angle to the XY-plane produces Z-axis errors due to motions in the X- and Y-axes, the T3 tilt angles produce X- and Y-axis errors due to motions in the Y- and X-axes, respectively, and the center location errors are absolute errors in the X- and Y-axes. The part has dimensions of approximately 100 mm in the X and Y-axis directions; therefore, the compensation routine reduced errors resulting from the angle to XY-plane from 9.18 μm to 3.75 μm and the errors resulting from the T3 tilt angle from 24.4 μm to 1.57 μm. The compensation algorithm was able to significantly reduce thermal-induced errors in the X-axis direction as seen by the change in center locations of both T3 and T4 in Table 3. The compensated errors were well within the measurement uncertainty. The center location errors along the Y-axis direction for T3 were within the measurement uncertainty for both E-II and E-III. However, the compensation algorithm was able to change the center location error along the Y-axis direction for T3 from 9.4 μm to 0.5 μm. In all cases, the compensation algorithm held thermal-induced errors within the measurement uncertainty.

5. Experimental study using Method II

5.1. Experimental setup and data collection process

This experimental study was conducted to demonstrate the measurement approach on a larger MIC6 aluminum workpiece, shown in Fig. 19(a). The experiments were performed on a Haas DM-1 vertical machining center (X/Y/Z travels: 508/406/394 mm, axis resolution: 2.54 μm). The workpiece setup is shown in Fig. 19(b).

For fixturing convenience, the fiducials and workpiece were all attached to an aluminum carrier plate, which essentially acts as the worktable for this experiment. This also has the added benefit that the coefficient of thermal expansion is equal for the workpiece, fiducial mounts, and carrier plate. This removes the need to compensate for ambient shifts causing different expansions in the workpiece and machine frame. However, the carrier plate is not a fundamental part of the proposed method. In many applications (e.g., the previous experimental study) the fiducials would instead be attached directly to the machine table in convenient and low-profile positions and would thus act as fixed references which would not need to be relocated for different part designs.

The same experimental procedures were run as the Method-I studies described in Fig. 16. Each test case was repeated three times for a total of nine machined parts. The warmup cycle continuously moved the X, Y, and Z axes for 45 min in G00 rapid mode (30,000 mm/min). Coolant was used for all cuts to ensure proper chip evacuation (Blaser Synergy 735 at roughly 20% concentration). For this demonstration, the fiducials were left uncovered during machining since the high-pressure coolant on this machine could infiltrate the fiducial caps and the chromium-on-glass fiducials would not be damaged by coolant exposure. Since contamination by coolant could affect the microscope measurements, each target was cleaned thoroughly using ethanol and a flashlight was used to check each fiducial for coolant residue before measurement. This cleaning procedure took roughly one minute to perform. The microscope was warmed up for 45 min before each experiment to reach thermal equilibrium and was left on for the duration of each experiment to maintain a consistent thermal state. Each part was measured with a Mitutoyo BH-710 CMM.

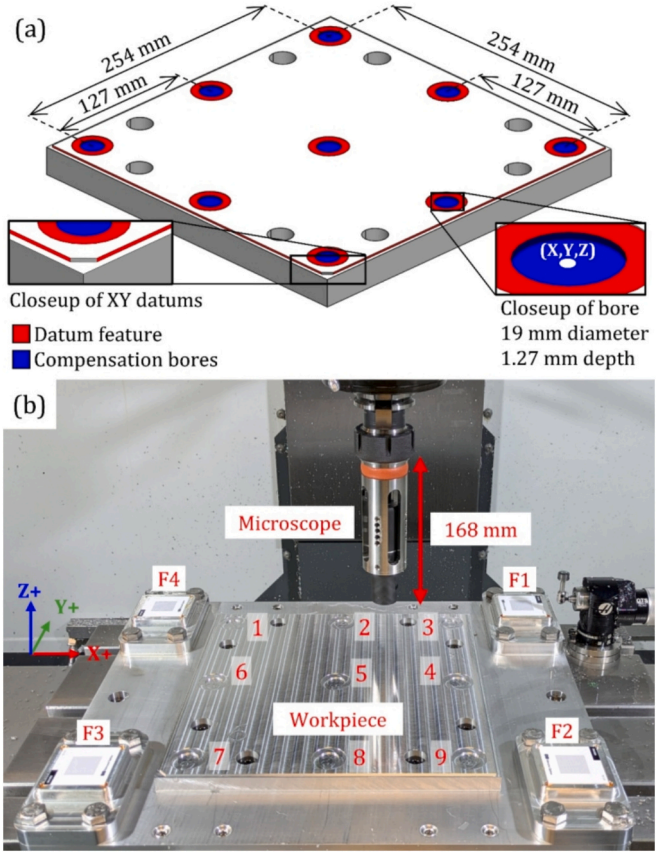

Fig. 19. (a) Artifact design for compensation tests. (b) Workpiece set up on machine tool. Numbers indicate order bores were machined in.

Fig. 19(a) illustrates the MIC6 aluminum artifact and its features used for validating the thermal drift compensation. The machining process was performed in two operations. First, the datum features were machined, and the compensation bores were rough machined (leaving 152 μm of stock). Second, the compensation bores were finished after no warmup (E-I), warmup without compensation (E-II), or warmup with compensation (E-III). Relative shifts between the datums and compensation bores reflect changes in the machine tool thermal state between the two operations, which was tracked by measuring F1 ~ F4 with the microscope before each operation (see M1 and M2 in Fig. 16). Each compensation bore defines an XYZ point, with X and Y specified by the center of the bore diameter and Z specified by the bottom of the bore. This part design therefore shows three-axis thermal drifts at nine locations on the part surface. Fig. 19(b) shows a machined workpiece on the machine tool.

5.2. Results

The measured thermal drifts are shown in Fig. 20, which represents the relative shift between the first M1 measurement (before machining the datum features) and the second M2 measurement (before machining the compensation bores). The E-I case exhibited minimal drift, with a maximum of 5 μm. In contrast, the E-II and E-III cases had up to 47 μm of the drifts in X, 108 μm in Y, and 16 μm in Z in the MCF. These results are generally similar between E-II and E-III, indicating that the warmup process produces reasonably similar thermal deformations in the machine.

Fig. 21 shows the CMM measurements for the E-II and E-III cases. Bore numbers reflect the order in which the features were machined (see Fig. 19(b)). For E-II, the maximum observed position error relative to E-I were -33 ± 2 μm for X, 87 ± 5 μm for Y, and 2 ± 2 μm for Z (Type A, $k =$

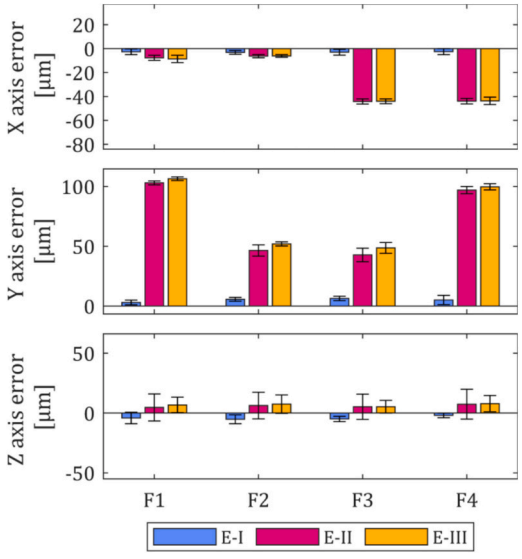

Fig. 20. Measured thermal drifts for Method-II experimental study from the microscope. Error bars show the standard deviation from all three repetitions (±1σ). All subplots are in different vertical ranges but have the same scales. E-I has small thermal drifts, with a maximum of 5 μm. E-II and E-III show larger thermal drifts up to 108 μm due to the warmup cycle. Note there was no compensation implemented during these tests.

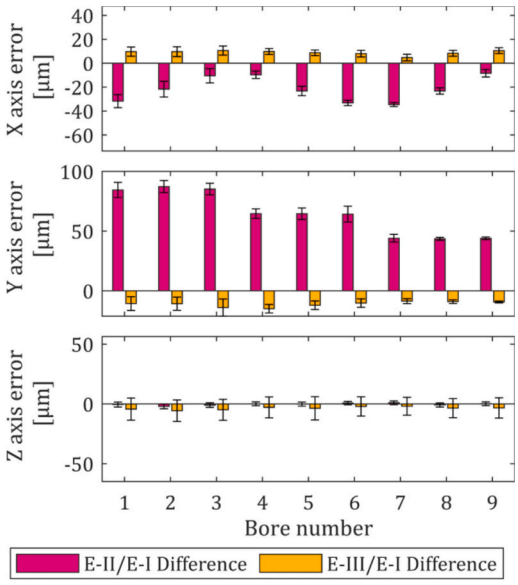

Fig. 21. Bore positioning deviations for second experiment, measured using CMM. Error bars show the standard deviation from all three repetitions (±1σ). All subplots are in different vertical ranges but have the same scales. E-II shows errors of up to 87 μm, while E-III has errors up to 15 μm.

1). For E-III, the maximum observed position error relative to E-I were 10.6 ± 4 μm for X, −15 ± 4 μm for Y, and −5.67 ± 9 μm for Z (Type A, $k = 1$).

5.3. Uncertainty analysis

Table 4 shows the sources of measurement uncertainty for the experimental study. The microscope and machine tool uncertainties were measured using capacitance probes with sub-micrometer uncertainty. Thus, the microscope uncertainty is inclusive of variability in both the microscope and the image processing algorithms. This uncertainty analysis assumes that the fiducials are clean and free from coolant and chips prior to each measurement, which can be accomplished either by removable caps or by cleaning prior to measurement.

The influence of centrifugal forces on the measurement due to the increased spindle rotation speed was analyzed by taking measurements at speeds varying from 3 rpm to 20 rpm, as shown in Fig. 22. Each measurement was repeated five times to establish uncertainties. The

Table 4
Uncertainty budget for Method-II experimental study. All uncertainties are modeled as normal distributions with a coverage factor of $k = 2$.

Component	Variable	Uncertainty
Microscope + data analysis (type A)	σ_{mscope}	XY: 1.5 μm Z: 6.4 μm
Microscope centrifugal forces (type A)	$\sigma_{centrigual}$	XY: 0.5 μm Z: 0 μm
Machine tool axes (type A)	$\sigma_{machine}$	3.0 μm
Spindle/microscope heating (type A)	$\sigma_{spindle}$	XY: 0.5 μm Z: 4.5 μm
Tool-change repeatability (type A)	σ_{taper}	XY: 1.0 μm[a] Z: 1.1 μm
Relative thermal drift measurement (type B)	σ_{drift}	XY: 5.0 μm Z: 11.9 μm
CMM (type B)	σ_{CMM}	1.4 μm
Feature quality (type B)	$\sigma_{feature}$	1.0 μm
CMM feature inspection (type B)	σ_{insp}	2.4 μm
Compensated thermal drift inspection (type B)	$\sigma_{drift.insp}$	XY: 5.5 μm Z: 12.1 μm

[a] XY tool change repeatability does not contribute to measurement uncertainty and is included for reference only.

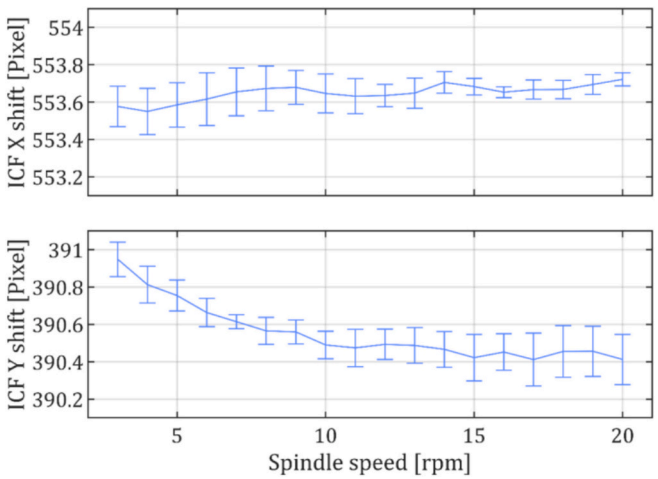

Fig. 22. Identified spindle centerline coordinates in the ICF as a function of rotation spindle speed. Error bars show ±1 standard deviation based on five repetitions. Increasing the spindle speed from 3 rpm to 20 rpm causes a 0.5 pixel shift in the rotation center due to centrifugal effects.

vibrations and centrifugal force from the increased rotation speed cause the rotation center to shift by up to 0.5 pixels. This mean shift does not affect the measurement accuracy provided the rotation center is stable and provides a consistent reference across images. The uncertainty in the center of rotation also remains fairly constant as a function of spindle speed, with the uncertainties in the ICF X- and Y-directions varying from 0.1 pixels and 0.08 pixels, respectively, at 3 rpm to 0.04 pixels and 0.13 pixels, respectively, at 20 rpm (type B, normal distribution, 1 standard deviation). Since the pixel length is approximately 1.6 μm, this translates to a maximum uncertainty of 0.21 μm to the center of rotation.

Tool-change repeatability for a CAT40 spindle was measured with capacitance probes: however, note that the XY tool-change repeatability does not affect the measurements. There is no fiducial installation uncertainty because they are never removed from the carrier plate.

All measurements are taken with the microscope assembly at thermal equilibrium with respect to the ambient temperature and internal heating from the microscope electronics. However, there are some transient thermal effects introduced by heat conducted from the machine spindle. These were quantified by ramping the spindle speed up to 10,000 rpm over the course of 20 min and then loading the microscope and running continuous measurements over one target for five minutes. Since the microscope will never be loaded for longer than this during actual measurements, this reflects an upper bound for the spindle/microscope heating.

Each thermal drift measurement is based on the relative displacement between two uncorrelated microscope measurements, so the total expanded uncertainty of the on-machine thermal drift measurement, σ_{drift}, is

$$\sigma_{drift} = \sqrt{2 \cdot \left(\sigma_{mscope}^2 + \sigma_{machine}^2 + \sigma_{centriful}^2 + \sigma_{spindle}^2 + \sigma_{taper}^2\right)} \tag{14}$$

This yields 5.0 μm for the X- and Y-axes and 11.9 μm for the Z-axis (Type B, $k = 2$). This is the uncertainty when a user is measuring and compensating thermal errors with the microscope system and applies to the data in Fig. 20.

The CMM repeatability was based on repeated measurements of a calibrated gage ring. The feature quality uncertainty is based on flatness and roundness errors in the machined features. Similar to the thermal drift measurements, the CMM feature inspection is based on the relative displacement between two uncorrelated CMM measurements. Hence, the total expanded uncertainty of the CMM feature inspection is

$$\sigma_{insp} = \sqrt{2 \cdot \left(\sigma_{CMM}^2 + \sigma_{feature}^2\right)} \quad (15)$$

This uncertainty applies to the E-II/E-I data in Fig. 20.

The total expanded uncertainty of the compensated thermal drift inspection includes the uncertainties due to on-machine microscope measurements and CMM measurements. Thus, the total $k = 2$ expanded uncertainty of the compensated thermal error inspection is

$$\sigma_{drift,insp} = \sqrt{\sigma_{drift}^2 + \sigma_{insp}^2} \quad (16)$$

This yields 5.5 μm for the X- and Y-axes and 12.1 μm for the Z-axis (Type B, $k = 2$). This is the uncertainty for the final inspected dimension when a user is compensating a feature and validating the effectiveness of the compensation via CMM inspection. The compensated thermal drift inspection applies to the E-III/E-I data in Fig. 20.

5.4. Discussion

The compensation method was successful at reducing the part error magnitudes, as shown in Fig. 22. For the X and Y directions, the compensation successfully reduced the part errors from a peak of 87 μm in E-II to only 15 μm in E-III, a reduction of 83%. This result, coupled with the low uncertainty for the microscope measurements, demonstrates the potential of the proposed approach.

The measured thermal drifts do show relatively large variability, as seen in the error bars in Fig. 21. For example, the three F2 drifts measured during the E-II test case varied by 11 μm in X and Y and 21 μm in Z, which is significantly larger than expected based on σ_{comp} in the uncertainty analysis in Section 5.3. This discrepancy is assigned to variability in the machine tool thermal state. While the warmup cycle was consistent for each run, it is likely that the thermal drifts were not exactly the same every time (similar to the experimental study in Section 4.3). Therefore, the error bars in Fig. 20 combine both the uncertainty associated with the microscope measurements and variability in the machine thermal state (which will then affect the dimensions of the final machined part).

While the compensation was generally successful, the E-III dataset shown in Fig. 21 does show two issues. First, the E-III experiments show some bias which causes mean offsets of 9 μm for X and − 11 μm for Y. These biases are attributed primarily to the small time constant for the machine tool, specifically for the machine tool's built-in thermal compensation algorithm. This algorithm cannot be edited or deactivated by the machine tool operators; however, all experiments were conducted with the algorithm activated. Therefore, the measured and compensated errors during tests E-I, E-II, and E-III were the residual components of the machine tool's built-in thermal compensation algorithm. Monitoring this compensation showed shifts greater than 5 μm between the beginning of the second measurement cycle and the end of the compensation feature machining. This occurred despite efforts to return the machine to its thermal steady state after the M2 measurement, and efforts to speed up the measurement and data processing to less than 2 min. This shift in controller compensation explains most of the observed biases. Furthermore, the machine controller compensation was generally repeatable between experiments, with compensation values under nominally identical thermal states repeating to roughly 5 μm. Since this is much smaller than the difference between the E-II and E-III results, the improvement in part accuracy in E-III is attributed primarily to the effect of the G-code modification rather than variation in the built-in thermal compensator.

The second issue is that the E-III parts show higher errors and variability compared with the E-II parts. This extra variability is caused by the low magnitude of the Z-axis thermal error compared with the Z-axis measurement uncertainty. This causes the microscope uncertainty to dominate the compensation, resulting in essentially random compensation moves.

Therefore, while this demonstration shows that the microscope measurements can successfully reduce the overall effect of thermal drift on part accuracy, the approach has several limitations which require further research. First, the contrast measurements are affected by coolant and chip contamination, which would be prevalent in industrial applications. Second, the Z-axis measurements can show large uncertainty which is not suitable for high-precision machining applications. Third, the measurement system cannot account for transient thermal states which shift during and after the microscope measurements. Future studies will work to mitigate these limitations by increasing the measurement and compensation speed, making the system more resilient to realistic industrial environments (e.g., by designing removable caps which are secure against high-pressure coolant or by studying the suitability of compressed air cleaning for different types of coolant), and modeling and compensating the effect of the machine tool time constant.

6. Conclusions and future work

6.1. Conclusions

This study proposed an in-process measurement and compensation strategy for machine tool thermal-induced errors. Two separate methods were conducted to improve the measurement and calculation speed to make the approach suitable for in-process measurement and compensation. Both methods were experimentally validated by using them to compensate for thermal drifts and evaluating the accuracy of the machined components. The machining results showed that the proposed strategy can decrease thermal-induced machining errors by up to an order of magnitude and demonstrated effectiveness in 2.5-axis machining.

The proposed strategy has multiple advantages over prior thermal error measurement and compensation methods. Specifically, this method (1) uses only one inexpensive camera/microscope, (2) mitigates spindle taper repeatability errors by measuring the thermal drifts relative to the rotation centerpoint, (3) can be utilized on machine tools currently in-service, (4) may be used with low-precision fiducials, (5) determines thermal drifts of four fiducials within two minutes, and (6) measures and compensates the thermal errors occurring in long-duration machining operations.

6.2. Future work

In the future, an integrated measurement method combining Method I and Method II will be investigated, and the method will be extended to machine tools with larger work volumes by increasing the number of fiducials and optimizing their locations, including multiple Z-axis heights. Further measurement uncertainty analysis, especially for the measurement of Z-axis drifts, will be conducted. Additionally, the measurement and compensation of large gantry machine tools having large, complex thermal deformations will be studied. To develop a more precise measurement, the fiducials will be fabricated with materials that have low coefficient of thermal expansion. Until now, the authors only implemented experiments where thermal deformation was due solely to the machine tool's heat sources. In the future, the capability for measuring and compensating thermal-induced errors caused by ambient temperature variations will be investigated, as well as the ability to compensate for static positioning errors induced by other sources (e.g., shifts in machine kinematic errors over long time periods).

To apply the thermal measurement and compensation strategy in industrial settings, the hardware and software will need to be industrial grade. Currently, the fiducials are covered and sealed to prevent them from being damaged during machining. More efficient, automated methods for cleaning off the residual coolant and chips and removing and placing covers will be developed. Microscope holders allowing them to be added to tool magazines will be investigated and the software, including graphical user interfaces, will be created.

CRediT authorship contribution statement

Zongze Li: Writing – original draft, Visualization, Investigation, Conceptualization. **Aaron Cornelius:** Writing – original draft, Visualization, Validation, Investigation. **Gonzalo Reyes:** Visualization, Validation. **Edward C. Kinzel:** Writing – review & editing, Resources. **Ryuta Sato:** Software, Resources. **Gregory W. Vogl:** Writing – review & editing, Methodology, Conceptualization. **Robert G. Landers:** Writing – review & editing, Supervision, Project administration.

Declaration of competing interest

Certain commercial equipment, instruments, or materials are identified in this paper in order to specify the experimental procedure adequately. Such identification is not intended to imply recommendation or endorsement by NIST, nor is it intended to imply that the materials or equipment identified are necessarily the best available for the purpose. This material is declared a work of the U.S. Government and is not subject to copyright protection in the United States. Approved for public release; distribution is unlimited.

The authors declare that they have no known competing financial interests or personal relationships that could have appeared to influence the work reported in this paper.

Acknowledgement

The authors would like to express the appreciation for the support from the following financial assistance award: 70NANB22H180 from the U.S. Department of Commerce, National Institute of Standards and Technology (NIST). The authors also would like to acknowledge Ryota Kawai, the student in Nagoya University, who helped to operate CMM measurements. Jared Tarr (Production Systems Group at NIST) and Jarred Nace, Mike Beacham, Mark Hutton, and Jay Nanninga (Fabrication Technology Office at NIST) are also thanked for their vital assistance with the experimental setup and CMM measurements.

Appendix A. Error model and parameter determination

The nine-parameter error model is formulated as

$$\mathbf{M}=\begin{bmatrix}1 & & & \\ \Delta E_{X0Y} & 1 & & \\ & & 1 & \\ & & & 1\end{bmatrix}\begin{bmatrix}1 & -\Delta E_c & \Delta E_B & \Delta E_X \\ \Delta E_C & 1 & -\Delta E_A & \Delta E_Y \\ -\Delta E_B & \Delta E_A & 1 & \Delta E_Z \\ & & & 1\end{bmatrix}\cdot\begin{bmatrix}(1+\Delta\alpha_X) & & & \\ & (1+\Delta\alpha_Y) & & \\ & & 1 & \\ & & & 1\end{bmatrix} \tag{A.1}$$

where the parameters are illustrated in Fig. 4(b) and described in Table 2.

A sensitivity matrix, which consists of the coordinates of the Fm positions in the MCF, is built to determine the error parameters from the measured thermal drifts. If the number of Fm is N_F, then the sensitivity matrix is

$$\mathbf{S}=\begin{bmatrix}1 & & & & -y_{(1)} & -y_{(1)} & x_{(1)} & \\ & 1 & & & x_{(1)} & & & y_{(1)} \\ & & 1 & y_{(1)} & -x_{(1)} & & & \\ 1 & & & & -y_{(2)} & -y_{(2)} & x_{(2)} & \\ & 1 & & & x_{(2)} & & & y_{(2)} \\ & & 1 & y_{(2)} & -x_{(2)} & & & \\ & & & \vdots & & & & \\ 1 & & & & -y_{(N_F)} & -y_{(N_F)} & x_{(N_F)} & \\ & 1 & & & x_{(N_F)} & & & y_{(N_F)} \\ & & 1 & y_{(N_F)} & -x_{(N_F)} & & & \end{bmatrix} \tag{A.2}$$

where $\left[x_{(i)}, y_{(i)}\right]$ represents the position coordinates of Fm i ($i=1\sim N_F$) in the MCF. The error model parameters are

$$\mathbf{e}=\mathbf{S}\backslash\begin{bmatrix}\Delta x_{M,(1)} & \Delta y_{M,(1)} & \Delta z_{M,(1)} \\ \Delta x_{M,(2)} & \Delta y_{M,(2)} & \Delta z_{M,(2)} \\ & \vdots & \\ \Delta x_{M,(N_F)} & \Delta y_{M,(N_F)} & \Delta z_{M,(N_F)}\end{bmatrix} \tag{A.3}$$

where $\left[\Delta x_{M,(i)}\ \Delta y_{M,(i)} \Delta z_{M,(i)}\right]^T$ represents the measured thermal drifts in the MCF of Fm i ($i=1\sim N_F$). The origin of the MCF is the machine tool origin. $\mathbf{e}$ in Eq. (A.3) is the vector of error parameters

$$\mathbf{e}=\left[\Delta E_X \quad \Delta E_Y \quad \Delta E_Z \quad \Delta E_A \quad \Delta E_B \quad \Delta E_C \quad \Delta E_{X0Y} \quad \Delta\alpha_X \quad \Delta\alpha_Y\right]^T \tag{A.4}$$

Appendix B. Demonstration of 2D-FFT algorithm

The grayscale color index values of each pixel in the i^{th} images ($i=1$ or 2) are transformed into the frequency domain using a 2D-FFT

$$\mathbf{F}_i(u+1,v+1)=\sum_{p_x=0}^{M-1}\sum_{p_y=0}^{N-1}\mathbf{f}_i\left(p_x+1,p_y+1\right)\exp\left(-2\pi\left(\frac{up_x}{M}+\frac{vp_y}{N}\right)\mathbb{i}\right), u=0\sim M-1, v=0\sim N-1 \tag{B.1}$$

where $\mathbf{f}_i\left(p_x, p_y\right)$ are the grayscale color index values of the pixel in the $p_x{}^{\text{th}}$ row and $p_y{}^{\text{th}}$ column of the i^{th} image, having a resolution of 256, M and N are the number of pixels in the X- and Y-directions, respectively, u and v are the discrete frequency indices in row and column directions, respectively, and $\mathbb{i} = \sqrt{-1}$.

Fig. B.1 shows Images 1 and 2 in the pixel and frequency domains from an experimental test (details given below) to identify the orientation of the MCF X-axis in the ICF. The difference between the images in Fig. B.1(a) and (b) is a shift in their pixels; therefore, their amplitude frequency responses are nearly identical while their phase frequency responses are different, as indicated by the red dashed boxes. If the displacement between Images 1 and 2 in the X- and Y-directions, respectively, is $\left(\Delta p_x, \Delta p_y\right)$, then

$$\mathbf{f}_2\left(p_x, p_y\right) \approx \mathbf{f}_1\left(p_x - \Delta p_x, p_y - \Delta p_y\right) \tag{B.2}$$

and the relationship between Images 1 and 2 in the frequency domain is

$$|\mathbf{F}_2(u,v)|\exp(\boldsymbol{\phi}_2(u,v)\mathbb{i}) = |\mathbf{F}_1(u,v)|\exp\left(\left(\boldsymbol{\phi}_2(u,v) - 2\pi\left(\frac{u\Delta p_x}{M} + \frac{v\Delta p_y}{N}\right)\right)\mathbb{i}\right), u = 1 \sim M, v = 1 \sim N \tag{B.3}$$

From Eq. (B.3), $|\mathbf{F}_1(u,v)| = |\mathbf{F}_2(u,v)|$ and the phase difference is

$$\Delta\boldsymbol{\phi}(u,v) = \boldsymbol{\phi}_2(u,v) - \boldsymbol{\phi}_1(u,v) = -2\pi\left(\frac{u\Delta p_x}{M} + \frac{v\Delta p_y}{N}\right) \tag{B.4}$$

To isolate the phase difference, the cross-power spectrum $\mathbf{C}_f(u,v)$ is computed

$$\mathbf{C}_f(u,v) = \frac{\mathbf{F}_1(u,v)\mathbf{F}_2^*(u,v)}{|\mathbf{F}_1(u,v)||\mathbf{F}_2(u,v)|} = \frac{|\mathbf{F}_1(u,v)|^2\exp(\boldsymbol{\phi}_1(u,v)\mathbb{k} - \boldsymbol{\phi}_2(u,v)\mathbb{i})}{|\mathbf{F}_1(u,v)||\mathbf{F}_2(u,v)|} = \exp(-\Delta\boldsymbol{\phi}(u,v)\mathbb{i}) \tag{B.5}$$

where * denotes the complex conjugate. The inverse Fourier transform of $\mathbf{C}_f(u,v)$ is

$$\mathbf{C}_{inv}\left(p_x, p_y\right) = \frac{1}{MN}\sum_{u=0}^{M-1}\sum_{v=0}^{N-1}\mathbf{C}_f(u+1, v+1)\exp\left(2\pi\left(\frac{up_x}{M} + \frac{vp_y}{N}\right)\mathbb{i}\right) \tag{B.6}$$

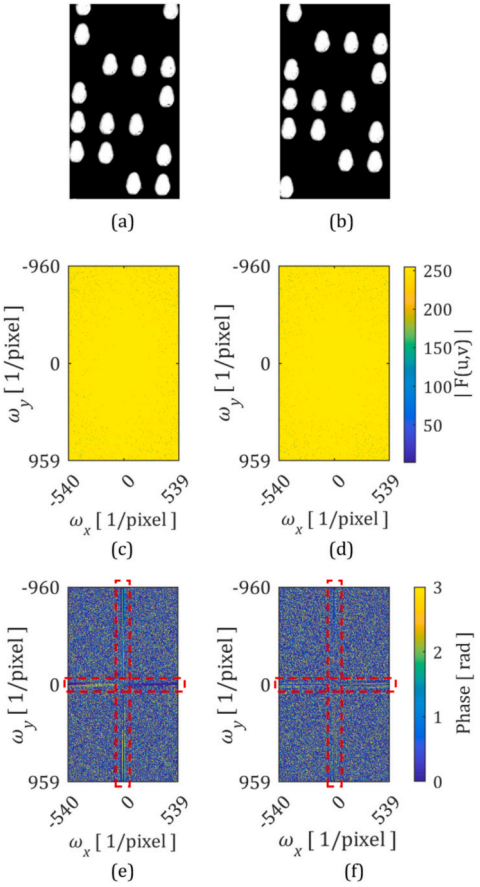

Fig. B.1. (a) and (b) Camera images of Images 1 and 2, respectively, (c) and (d) amplitude frequency responses of Images 1 and 2, respectively, and (e) and (f) phase frequency responses of Images 1 and 2, respectively. Red boxes indicate significant differences in phase frequency responses.

Ideally, $\mathbf{C}_{inv}$ is a one-hot matrix and the pixel shift indicators between the two images, denoted $\left(p_{x0}, p_{y0}\right)$, is such that $\mathbf{C}_{inv}\left(p_{x0}, p_{y0}\right) = 1$. Comparing Fig. B.1(a) and (b) as an example, at the image edges some patterns have left the image view while some patterns have entered the image view. This creates noise and, as a result, $\mathbf{C}_{inv}$ is not a perfect one-hot matrix, as shown in Fig. B.2. Therefore, the pixel shift indicator is

$$\left(p_{x0}, p_{y0}\right) = \underset{\left(p_x, p_y\right)}{\operatorname{argmax}} \mathbf{C}_{inv}\left(p_x, p_y\right) \tag{B.7}$$

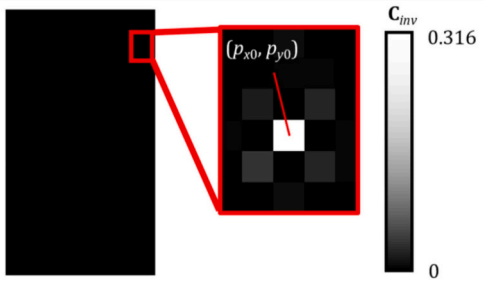

Fig. B.2. Calculated $\mathbf{C}_{inv}(p_x,p_y)$ from Fig. B.1(a) and (b), which is not a perfect one-hot matrix. The hot pixel indices $\left(p_{x0}, p_{y0}\right)$ is the pixel shift indicator.

The positive and negative frequencies correspond to positive and negative translations, respectively. The pixel displacement between the two images is

$$\Delta p_x = \begin{cases} p_{x0} - 1 & p_{x0} \le \dfrac{M}{2} \\ p_{x0} - \dfrac{M}{2} - 1 & p_{x0} > \dfrac{M}{2} \end{cases} \quad \Delta p_y = \begin{cases} p_{y0} - 1 & p_{y0} \le \dfrac{N}{2} \\ p_{y0} - \dfrac{N}{2} - 1 & p_{y0} > \dfrac{M}{2} \end{cases} \tag{B.8}$$

Appendix C. Algorithm of contrast-based method to determine the out-of-plane deviation

A contrast value is utilized to determine vertical differences between images. The contrast value of the i^{th} image at State j, based on the Gaussian derivative method, is

$$\psi^{(j)} = \frac{1}{MN} \sum_{p_x=1}^{M} \sum_{p_y=1}^{N} \mathbf{\Phi}_i^{(j)}\left(p_x, p_y\right) \tag{C.1}$$

where

$$\mathbf{\Phi}_i^{(j)}\left(p_x, p_y\right) = \left(\sum_{\hat{x}=-N_w}^{N_w} \sum_{\hat{y}=-N_w}^{N_w} \mathbf{\Gamma}_{\hat{x}}(\hat{x},\hat{y}) \mathbf{f}_i^{(j)}\left(p_x - \hat{x}, p_y - \hat{y}\right) \right)^2 + \left(\sum_{\hat{x}=-N_w}^{N_w} \sum_{\hat{y}=-N_w}^{N_w} \mathbf{\Gamma}_{\hat{y}}(\hat{x},\hat{y}) \mathbf{f}_i^{(j)}\left(p_x - \hat{x}, p_y - \hat{y}\right) \right)^2 \tag{C.2}$$

and the Gaussian derivative spectrum $\mathbf{\Gamma}(x,y)$ is

$$\mathbf{\Gamma}(\hat{x},\hat{y}) = \frac{1}{2\pi\sigma} \exp\left(-\frac{\hat{x}^2 + \hat{y}^2}{2\sigma^2} \right) \quad \begin{cases} -N_w \le \hat{x} \le N_w \\ -N_w \le \hat{y} \le N_w \end{cases} \tag{C.3}$$

where $N_w = 7$ is half of the Gaussian convolution kernel, $\sigma = N_w/2.5$, and $\mathbf{\Gamma}_x$ and $\mathbf{\Gamma}_y$ are the partial derivatives of the Gaussian derivative spectrum $\mathbf{\Gamma}(x,y)$ with respect to x and y, respectively. Note that N_w and σ are typical values used in the Gaussian derivative method [37].

For constant ambient lighting, the contrast metric is maximum when the image is in focus. Before thermal deformation, (i.e., State 1), several images of the measurement fiducial are taken around the original position for different Z-positions, denoted $\mathbf{z} = [z_1, z_2, \ldots, z_{N_z}]$, where N_z is the number of images, which is an odd number such that $z_{(1+N_z)/2}$ is the original position. The data are fit to create a contrast metric curve at State 1, denoted $\mathbf{\Psi}^{(1)}$. After thermal deformation, (i.e., State 2), the microscope takes N_z images at the same positions $\mathbf{z}$. Again, the data at State 2 are fit to a contrast metric curve, denoted $\mathbf{\Psi}^{(2)}$. The out-of-plane deviation between States 1 and 2 is determined by comparing the contrast metric curves. Due to potential changes in the lighting conditions between measurements, the contrast metric curve $\mathbf{\Psi}^{(2)}$ is rescaled to the contrast metric curve $\widehat{\mathbf{\Psi}}^{(t)}$

$$\widehat{\mathbf{\Psi}}^{(2)} = \frac{\max\left(\mathbf{\Psi}^{(2)}\right)}{\max\left(\mathbf{\Psi}^{(2)}\right)} \mathbf{\Psi}^{(2)} \tag{C.4}$$

The Z-axis error between the two states is determined by aligning the contrast metric curves. The contrast metric curve $\widehat{\mathbf{\Psi}}^{(2)}$ is shifted along the Z-axis within the range $[-z_R, z_R]$ by increments of d_z, where z_R is a threshold value indicating the Z-axis measurement range. The range must be smaller

than $(z_{N_z} - z_1)/2$ as the peak value of $\mathbf{\Psi}^{(1)}$ is usually near $(z_{N_z} - z_1)/2$. The Z-axis thermal-induced error is

$$\Delta z_M = \underset{\Delta z}{\operatorname{argmin}}\left(\mathrm{RMS}\left(\mathbf{\Psi}^{(1)}(z) - \widehat{\mathbf{\Psi}}^{(2)}(z+\Delta z)\right)\right) \quad \min(0, \Delta z) \le z \le \max(z_{N_z}, z_{N_z} + \Delta z) \tag{C.5}$$

Appendix D. Supplementary data

Supplementary data to this article can be found online at https://doi.org/10.1016/j.jmapro.2026.05.074.

References

[1] Postlethwaite SR, Allen JP, Ford DG. Machine tool thermal error reduction—an appraisal. Proc Inst Mech Eng Part B J Eng Manuf 1999;213:1–9. https://doi.org/10.1177/095440549921300101.

[2] Mayr J, Jedrzejewski J, Uhlmann E, Alkan Donmez M, Knapp W, Härtig F, et al. Thermal issues in machine tools. CIRP Ann Manuf Technol 2012;61:771–91. https://doi.org/10.1016/j.cirp.2012.05.008.

[3] Anandan KP, Ozdoganlar OB. Analysis of error motions of ultra-high-speed (UHS) micromachining spindles. Int J Mach Tools Manuf 2013;70:1–14. https://doi.org/10.1016/j.ijmachtools.2013.02.005.

[4] Donmez MA, Hahn MH, Soons JA. A novel cooling system to reduce thermally-induced errors of machine tools. CIRP Ann Manuf Technol 2007;56:521–4. https://doi.org/10.1016/j.cirp.2007.05.124.

[5] Ramesh R, Mannan MA, Poo AN. Error compensation in machine tools — a review. Int J Mach Tools Manuf 2000;40:1257–84. https://doi.org/10.1016/S0890-6955(00)00010-9.

[6] Tan B, Mao X, Liu H, Li B, He S, Peng F, et al. A thermal error model for large machine tools that considers environmental thermal hysteresis effects. Int J Mach Tools Manuf 2014;82–83:11–20. https://doi.org/10.1016/j.ijmachtools.2014.03.002.

[7] Gomez-Acedo E, Olarra A, Orive J, Lopez De La Calle LN. Methodology for the design of a thermal distortion compensation for large machine tools based in state-space representation with Kalman filter. Int J Mach Tools Manuf 2013;75:100–8. https://doi.org/10.1016/j.ijmachtools.2013.09.005.

[8] Kang Y, Chang C-W, Huang Y, Hsu C-L, Nieh I-F. Modification of a neural network utilizing hybrid filters for the compensation of thermal deformation in machine tools. Int J Mach Tools Manuf 2007;47:376–87. https://doi.org/10.1016/j.ijmachtools.2006.03.007.

[9] Biermann D, Holtermann R, Menzel A, Schumann S. Modelling and simulation of thermal effects in internal traverse grinding of hardened bearing steel. CIRP Ann Manuf Technol 2016;65:321–4. https://doi.org/10.1016/j.cirp.2016.04.005.

[10] Shi H, Ma C, Yang J, Zhao L, Mei X, Gong G. Investigation into effect of thermal expansion on thermally induced error of ball screw feed drive system of precision machine tools. Int J Mach Tools Manuf 2015;97:60–71. https://doi.org/10.1016/j.ijmachtools.2015.07.003.

[11] Liu H, Miao EM, Wei XY, Zhuang XD. Robust modeling method for thermal error of CNC machine tools based on ridge regression algorithm. Int J Mach Tools Manuf 2017;113:35–48. https://doi.org/10.1016/j.ijmachtools.2016.11.001.

[12] Miao E, Liu Y, Liu H, Gao Z, Li W. Study on the effects of changes in temperature-sensitive points on thermal error compensation model for CNC machine tool. Int J Mach Tools Manuf 2015;97:50–9. https://doi.org/10.1016/j.ijmachtools.2015.07.004.

[13] Gao Q, Zhang P. The errors recognition and compensation for the numerical control machine tools based on laser testing technology. Open Phys 2019;17:857–62. https://doi.org/10.1515/phys-2019-0090.

[14] Ashok SD, Samuel GL. Modeling, measurement, and evaluation of spindle radial errors in a miniaturized machine tool. Int J Adv Manuf Technol 2012;59:445–61. https://doi.org/10.1007/s00170-011-3519-8.

[15] Straka M, Mareš M, Horejš O, Sulitka M, Je S, Kim H, Kim C-J. Study on applicability of touch trigger probes in issues of on-machine measurement of machine tool thermal errors. CIRP J Manuf Sci Technol 2025;63:522–32. https://doi.org/10.1016/j.cirpj.2025.11.004.

[16] Bitar-Nehme E, Mayer JRR. Thermal volumetric effects under axes cycling using an invar R-test device and reference length. Int J Mach Tools Manuf 2016;105:14–22. https://doi.org/10.1016/j.ijmachtools.2016.03.003.

[17] Yang S-H, Kim K-H, Park YK. Measurement of spindle thermal errors in machine tool using hemispherical ball bar test. Int J Mach Tools Manuf 2004;44:333–40. https://doi.org/10.1016/j.ijmachtools.2003.08.010.

[18] Ibaraki S, Blaser P, Shimoike M, Takayama N, Nakaminami M, Ido Y. Measurement of thermal influence on a two-dimensional motion trajectory using a tracking interferometer. CIRP Ann Manuf Technol 2016;65:483–6. https://doi.org/10.1016/j.cirp.2016.04.067.

[19] Mori M, Irino N, Shimoike M. A new measurement method for machine tool thermal deformation on a two-dimensional trajectory using a tracking interferometer. CIRP Ann Manuf Technol 2019;68:551–4. https://doi.org/10.1016/j.cirp.2019.04.093.

[20] Brecher C, Spierling R, Fey M, Neus S. Direct measurement of thermo-elastic errors of a machine tool. CIRP Ann Manuf Technol 2021;70:333–6. https://doi.org/10.1016/j.cirp.2021.04.084.

[21] Gomez-Acedo E, Olarra A, Zubieta M, Kortaberria G, Ariznabarreta E, López De Lacalle LN. Method for measuring thermal distortion in large machine tools by means of laser multilateration. Int J Adv Manuf Technol 2015;80:523–34. https://doi.org/10.1007/s00170-015-7000-y.

[22] Mutilba U, Yagüe-Fabra JA, Gomez-Acedo E, Kortaberria G, Olarra A. Integrated multilateration for machine tool automatic verification. CIRP Ann Manuf Technol 2018;67:555–8. https://doi.org/10.1016/j.cirp.2018.04.008.

[23] Ibaraki S, Ota Y. A machining test to calibrate rotary axis error motions of five-axis machine tools and its application to thermal deformation test. Int J Mach Tools Manuf 2014;86:81–8. https://doi.org/10.1016/j.ijmachtools.2014.07.005.

[24] Ibaraki S, Okumura R. A machining test to evaluate thermal influence on the kinematics of a five-axis machine tool. Int J Mach Tools Manuf 2021;163:103702. https://doi.org/10.1016/j.ijmachtools.2021.103702.

[25] Cheng T, Xiang S, Zhang H, Yang J. New machining test for identifying geometric and thermal errors of rotary axes for five-axis machine tools. Measurement 2023;223:113748. https://doi.org/10.1016/j.measurement.2023.113748.

[26] Mendikute A, Leizea I, Yagüe-Fabra JA, Zatarain M. Self-calibration technique for on-machine spindle-mounted vision systems. Measurement 2018;113:71–81. https://doi.org/10.1016/j.measurement.2017.08.029.

[27] Irino N, Shimoike M, Mori K, Yamaji I, Mori M. A vision-based machine accuracy measurement method. CIRP Ann Manuf Technol 2020;69:445–8. https://doi.org/10.1016/j.cirp.2020.04.107.

[28] Hartlieb S, Tscherpel M, Guerra F, Haist T, Osten W, Ringkowski M, et al. Highly accurate imaging based position measurement using holographic point replication. Measurement 2021;172:108852. https://doi.org/10.1016/j.measurement.2020.108852.

[29] Li X, Liu W, Pan Y, Liang B, Zhou M, Li H, et al. Monocular-vision-based contouring error detection and compensation for CNC machine tools. Precis Eng 2019;55:447–63. https://doi.org/10.1016/j.precisioneng.2018.10.015.

[30] Zhang H, Miao Y, Yan B, Li Q, Park G. Accurate phase-based 3D positioning for machine calibration using perspective-aligned gabor filter and monocular vision. Mech Syst Signal Process 2025;237:113074. https://doi.org/10.1016/j.ymssp.2025.113074.

[31] Vogl GW, Rexford A, Li Z, Landers RG, Kinzel EC, Donmez MA, et al. Vision-based thermal drift monitoring method for machine tools. CIRP Ann Manuf Technol 2023;72:301–4. https://doi.org/10.1016/j.cirp.2023.04.053.

[32] Li Z, Vogl GW, Kinzel EC, Santa B, Landers RG. Machine tool thermal error measurement and prediction via wireless microscope. Manuf Lett 2024;41:1440–51. https://doi.org/10.1016/j.mfglet.2024.09.171.

[33] Kamiguchi M, Maekawa S. CNC data correction method. USOO6167325A; 1997.

[34] Lei WT, Hsu YY. Accuracy enhancement of five-axis CNC machines through real-time error compensation. Int J Mach Tools Manuf 2003;43:871–7. https://doi.org/10.1016/S0890-6955(03)00089-0.

[35] Sato R, Hasegawa S, Shirase K, Hasegawa M, Saito A, Iwasaki T. Motion accuracy enhancement of five-axis machine tools by modified CL-data. Int J Automation Technol 2018;12:699–706. https://doi.org/10.20965/ijat.2018.p0699.

[36] Reddy BS, Chatterji BN. An FFT-based technique for translation, rotation, and scale-invariant image registration. IEEE Trans Image Process 1996;5:1266–71. https://doi.org/10.1109/83.506761.

[37] Pertuz S, Puig D, Garcia MA. Analysis of focus measure operators for shape-from-focus. Pattern Recognit 2013;46:1415–32. https://doi.org/10.1016/j.patcog.2012.11.011.

[38] Atherton TJ, Kerbyson DJ. Size invariant circle detection. Image Vision Comput 1999;17:795–803. https://doi.org/10.1016/S0262-8856(98)00160-7.

[39] EdMund Optics Stock #59-210 2025. https://www.edmundoptics.com/p/25-x-25mm-050mm-spacing-opal-distortion-target/15957/?srsltid=AfmBOopmE9j0N2drERvCfmsZveUd9EbFKPR7fNDyHSFKuIM156GYNWA0; 2006.

[40] ISO 10791-7: 2020, test conditions for machining centers – part 7: accuracy of finished test pieces. 2020.